

**PREDICTION OF OPTICAL TURBULENCE IN THE
STRATOSPHERE**

**Final Report on year 2 of Contract #F61708-97-C0005
United States Air Force, Sept. 1999**

by

N. S. Kopeika

Department of Electrical and Computer Engineering
Ben-Gurion University of the Negev
Beer-Sheva, Israel

Principal Investigator

19991105 110

AQFOO-02-0416

Introduction

This past period has been devoted to finalizing the lidar system design and ordering required equipment. A great deal of time was spent on studying characteristics and prices of intensified CCD systems. Such devices fill a critical need since they are to be used to determine angle of arrival fluctuations in actual images of the lidar returns from different elevations. They thus provide the basis for measuring the elevation profile of C_n^2 . Such a device is also the most expensive component of our planned lidar. Consequently, the decision as to which model to purchase from which company required several months of data discussion with different vendors. In the end, the Andor ICCD system manufactured by Andor Technology was chosen. Finally, all the major components of the lidar have been ordered, and most have already been delivered. The intensified CCD should arrive within two months.

In addition, a new lab was built for the lidar. The room is located on the roof of our department building and is characterized by two windows in the ceiling – one above the transmitter and one above the receiver. The structural changes have been completed.

The lidar system should be operational within a month or two. **Even though the project is now officially completed**, it is our intention to continue issuing progress reports on the data and analyses so that a great number of measurements can be taken and used to model accurately aerosol size distribution and turbulence strength vertical profiles for different seasons and times of day, and their effects on laser beam propagation at various altitudes.

These should provide more reliable and lasting data than the balloon measurements suggested in the original proposal. It should be noted that the balloons and Air Force crews to make the originally proposed measurements never arrived. The lidar measurements should provide more, better, and more reliable data than the originally proposed balloon measurements.

The lidar system and expected results are summarized in the following pages. These expected results are to be compared with the actual measurements. We will not be surprised if measurements in the Middle East prove to be somewhat different from those elsewhere. **In any event, as shown here the calculations based on data in the literature indicate that laser beam widening at elevations from 2 to 20 km caused**

by aerosols can be expected to be very significant, quite probably even more so than that caused by turbulence. Hence, in airborne laser weaponry it is most prudent to consider aerosol effects in system design and analyses of experiments.

1. Expected lidar returns.

The constituents in the atmosphere that interact with the transmitted laser pulse to produce the backscattered signal include the gaseous air molecules and aerosol particles. Molecules, because of their small size, scatter light rather weakly, producing Rayleigh scattering which varies inversely with the fourth power of wavelength of the incident radiation (actually $\lambda^{-4.0117}$). Atmospheric aerosol particles are polydisperse and span a wide particle size range (~0.01 to 10 micrometers) which includes the lidar wavelength range. Thus, aerosol particles strongly scatter/diffract light producing what is generally approximated as Mie scattering after the generalized spherical particle scattering theory. At a given lidar wavelength, molecular scattering varies directly with the atmospheric molecular number density, but aerosol scattering varies in a complicated manner depending on the size distribution, shape, and refractive index of the aerosol particles. Because aerosol particles are considerably larger than air molecules, aerosol backscatter is typically much less sensitive to wavelength. The aerosol scattering wavelength dependence is modeled as λ^{-x} , where x is the Angstrom coefficient (x typically varies between 1 and 2).

Table 1. Particles responsible for atmospheric scattering.

Type	Radius (μm)	Concentration (cm^{-3})
Air molecules	10^{-4}	10^{19}
Aitken nucleus ¹	10^{-3} - 10^{-2}	10^2 - 10^4
Haze particles ²	10^{-2} - 1	10 - 10^3
Fog droplets	1-10	10-100
Cloud droplets	1-10	10-300
Raindrops	10^2 - 10^4	10^{-5} - 10^{-2}

¹Salt, dust, pollen, etc.

²Small fog droplet.

Both molecular and aerosol scattering contribute to the atmospheric extinction (km^{-1}) and backscatter ($\text{km}^{-1} \text{sr}^{-1}$) coefficients

$$\sigma(z) = \sigma_R(z) + \sigma_a(z), \quad (1)$$

$$\beta(z) = \beta_R(z) + \beta_a(z),$$

where $\sigma_R(z)$, $\beta_R(z)$ and $\sigma_a(z)$, $\beta_a(z)$ are the Rayleigh (molecular) and aerosol extinction / backscattering coefficients, respectively.

The aerosol backscatter coefficient profile gives a direct indication of aerosol loading and qualitatively reflects the shape of the mass-concentration profile, whereas the surface-area-concentration profile is correlated with the extinction profile.

The backscatter ratio (R_s) is commonly used to characterize the relative contributions of molecular and aerosol scattering. R_s is defined as the total backscatter coefficient divided by the molecular backscatter coefficient:

$$R_s(z) = \frac{\beta_R + \beta_a}{\beta_R} = 1 + \frac{\beta_a}{\beta_R}. \quad (2)$$

The backscatter ratio is derived from the lidar profile of backscattered energy.

The molecular backscatter coefficient profile can be computed from theory using model atmosphere values for the temperature $T(z)$ (degrees Kelvin) and pressure $p(z)$ (millibars):

$$\beta_m(\lambda, z) = 3.6 \times 10^{-31} \cdot \lambda^{-4.0117} \cdot \frac{p(z)}{T(z)}. \quad (3)$$

The backscattering is optimal if the wavelength is of the order of magnitude of the mean particle radius. Thus at high altitudes the 355 nm return signal is much larger than the 532 and 1064 nm signals, even though the 355 nm laser pulse energy is smaller. Conversely, the 355 nm signal experiences more attenuation, and the longer wavelengths penetrate better to the lowest layers of the atmosphere. The wavelength dependence of the particle backscattering generally decreases with increasing particle size. In [1] shown that the ratio of the backscattering at 532 nm and 355 nm can be

used to discriminate between aerosol particles with different size in the upper troposphere. If a layer is composed of aerosols, then the ratio $\beta_{532} / \beta_{355}$ is significantly less than unity. If the layer is a thin cloud composed of ice crystals, which are much larger than aerosol particles, then $\beta_{532} / \beta_{355}$ is close to unity.

Table 2 shows the backscattering ratios for different laser wavelengths that were calculated for a visibility of 10 km using a continental aerosol distribution.

Table 2. Ratio of aerosol-to-molecular scattering.

Wavelength [μm]	Ratio
0.53	2.8
1.06	23
1.54	70
10.6	>2000

Another valuable aerosol quantity is the lidar ratio (R_L), defined as the ratio of aerosol-extinction coefficient to aerosol-backscatter coefficient at a given wavelength. This quantity can be used to locate regions of atmospheric aerosol layering and to provide information on the transmission and reflection properties of the atmosphere. It is a relative measure of aerosol size distribution with respect to height, with larger particles generally being represented by smaller lidar ratios. For instance, a change of the lidar ratio from 18 to 36 sr corresponds to a change of the effective radius from 0.35 to 0.18 μm .

The actual values of R_L for tropospheric aerosol may range from 28 to 48 sr (typical of rural atmosphere). In [2] were suggested values for the lidar ratio of 30 sr in the troposphere and 50 sr in the stratosphere. In [3] is given a lidar ratio of about 60 sr for small stratospheric liquid droplets with an effective radius of about 0.1 μm and of about 10 sr for cirrus ice crystals (10 to 1000 μm in size).

Radiative and microphysical properties of aerosols are variable in time and space.

The planetary boundary layer (PBL, 2-3 km) contains most of the aerosol and water vapor in the atmosphere. Aerosols in the PBL generally have the accumulation particle mode around 0.1-0.2 μm in radius and the large particle mode around several micrometers for volume size distribution. The large mode consists mainly of soil-derived particles or sea salt particles whereas the accumulation mode consists of

anthropogenic particles such as sulfates or nitrates. Maximal values of the individual modes change with season or with different atmospheric conditions.

Aerosols in the free troposphere (4-12 km) are from two main sources: aftermaths of major volcanic eruptions and desertic dust episodes. Studies of Saharan dust optical properties show that the wavelength dependence of the aerosol extinction coefficient is almost zero in the visible and the near UV owing to an enhancement of the number of large diameter particles ($>2 \mu\text{m}$).

The base of the stratospheric aerosol layer is usually at the tropopause (approximately 16 km). The main structure of the stratospheric aerosol profile, the Junge layer, is located a few km above the tropopause. Particles greater than a micrometer in size are more effectively removed from the stratosphere because of the Earth's gravitation.

Above the stratospheric aerosol layer, the laser backscatter becomes purely Rayleigh and can be related directly to molecular density.

Aerosol profiles are summarized in Table 3 [4].

The aerosol concentration is expressed in terms of extinction coefficients for a reference wavelength of $0.5 \mu\text{m}$. Depending on the aerosol type three to four different layers are considered. The first and second layers describe the distribution of aerosol in the troposphere. The third and the fourth layers indicate the vertical state of the tropospheric background aerosol and the stratospheric aerosol.

Maritime-mineral aerosols are considered differently, as the layer up to 4.5 km is divided into two layers. The first layer consists of pure maritime aerosols, while the second layer is populated by freshly produced dust. The extinction coefficient values in Table 3 refer to dry particles.

The aerosol size distribution for all types is given in [4,5,6], and in a previous report (December 1998).

Table 3. Vertical distribution of different atmospheric aerosol types.

σ_{eo} and $\sigma_e(h)$ give the extinction coefficient in km^{-1} for 10 m above ground and at a height h respectively. The quantity Z means the scale height for an exponential profile type.

Aerosol type	1. layer	2. layer	3. layer (trop. backgr.)	4. layer (stratosph.)
clean continental (rural)	0-2 km $\sigma_e(h)=\sigma_{eo}=0.126$	2-12 km 0.02-0.005		12-35 km 0.01-2E-4
average continental	0-2 km $\sigma_e(h)=\sigma_{eo}=0.22$	2-12 km 0.02-0.005		12-35 km 0.01-2E-4
desert (wintertime)	0-3 km $\sigma_e(h)=\sigma_{eo}=0.303$	3-12 km 0.02-0.005		12-35 km 0.01-2E-4
desert (summertime)	0-3 km $\sigma_e(h)=\sigma_{eo}=0.735$	3-12 km 0.025-0.005		12-35 km 0.012-2.5E-4
urban	0-2 km $\sigma_e(h)=\sigma_{eo}=0.436$	2-12 km 0.02-0.008		12-35 km 0.01-2.2E-4
clean maritime	0-3 km $\sigma_e(h)=\sigma_{eo} e^{-h/Z}$ $\sigma_{eo}=0.123,$ $Z=1 \text{ km}$	3-12 km 0.02-0.002		12-35 km 0.005-2E-4
maritime mineral	0-3 km $\sigma_e(h)=\sigma_{eo} e^{-h/Z}, \sigma_{eo}=0.342$ $\sigma_{eo}=0.125,$ $Z=1 \text{ km}$	3-4.5 km 0.03-0.005	4.5-12 km	12-35 km 0.008-2E-4
maritime polluted	0-3 km $\sigma_e(h)=\sigma_{eo} e^{-h/Z}$ $\sigma_{eo}=0.147,$ $Z=1 \text{ km}$		3-12 km 0.012-0.005	12-35 km 0.008-2E-4
Arctic aerosol	0-3.5 km $\sigma_e(h)=\sigma_{eo} e^{-h/Z},$ $\sigma_{eo}=0.317, Z=1.4 \text{ km}$		3.5-12 km 0.015-0.005	12-35 km 0.008-2E-4
Antarctic aerosol	0-10 km $\sigma_e(h)=\sigma_{eo} e^{-h/Z},$ $\sigma_{eo}=0.018, Z=3.5 \text{ km}$		10-12 km 0.002	12-35 km 2.2E-4

Fig. 1 shows the aerosol-extinction-coefficient profile derived from the measured lidar echoes [7]. *An increase in aerosol scattering of approximately one order of magnitude can be seen above the tropopause altitude.*

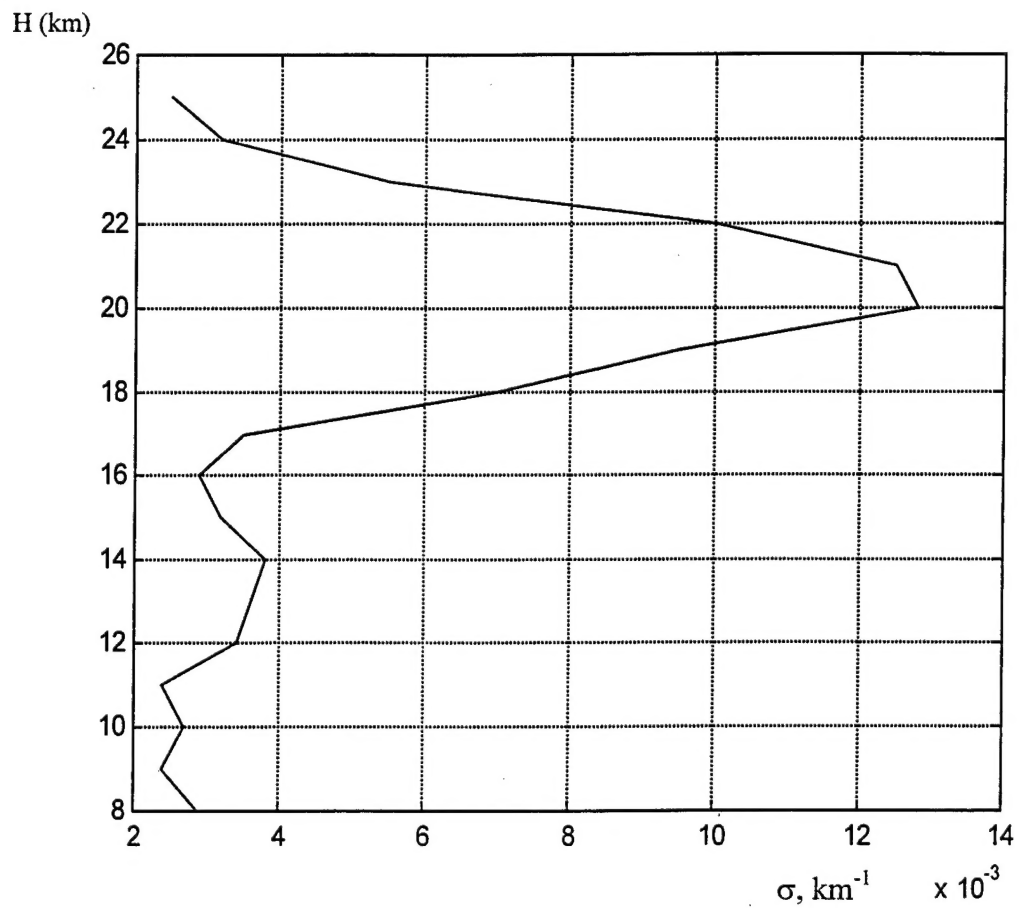


Fig. 1. Average aerosol extinction coefficient profile at 351 nm.

2. Atmospheric transmission and optical depth.

The laser irradiance in the target plane located at range z from the transmitter is given by

$$I(z) = \frac{P_L \cdot T(\lambda, z)}{\pi W^2(z)}, \quad (4)$$

$$W(z) = \sqrt{W_0^2 + \theta^2 \cdot z^2}, \quad (5)$$

where $W(z)$ represents the radius of the laser pulse in the target plane at the instant of interest, W_0 is the laser output aperture radius, θ is half the laser beam's divergence angle, P_L is the total output power of the laser, and $T(\lambda, z)$ is the atmospheric transmission at laser wavelength to range z . The distribution of laser irradiance across the target plane is assumed to be uniform over the area of illumination.

The transmission or attenuation factor $T(\lambda, z)$ follows the exponential law of attenuation, the Beer-Lambert law. It is related to the path optical depth or integrated extinction by

$$T(\lambda, z) = \exp(-\tau(\lambda, z)) \quad (6)$$

or

$$T(\lambda, z) = \exp\left(-\int_0^z \sigma(\lambda, z') dz'\right), \quad (7)$$

where $\tau(z)$ is the atmospheric optical depth through height z and $\sigma(z)$ is the atmospheric unit volume extinction coefficient (km^{-1}) at any intervening height z' between 0 and z . The extinction coefficient includes the loss effects of both scattering and absorption.

In Figs.2-7 the horizontal profiles of optical depth, atmospheric transmission and laser irradiance in the target plane for different aerosol types at different elevation heights are presented.

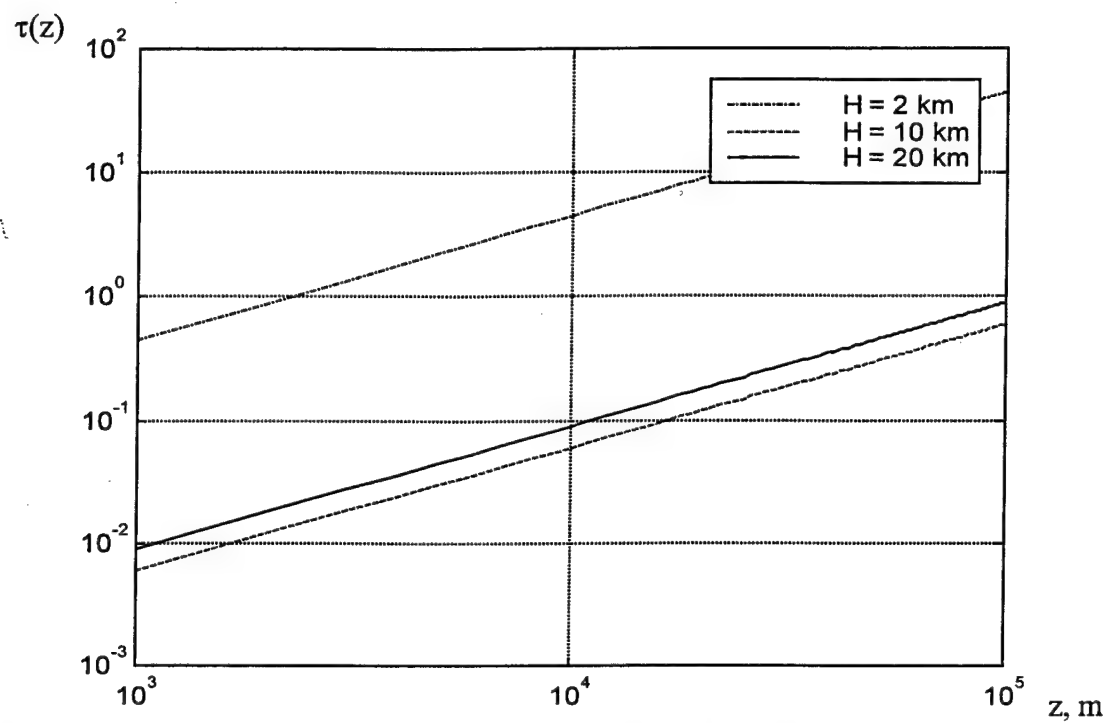


Fig.2. Horizontal profiles of optical depth at different elevation heights. Desert aerosol type.

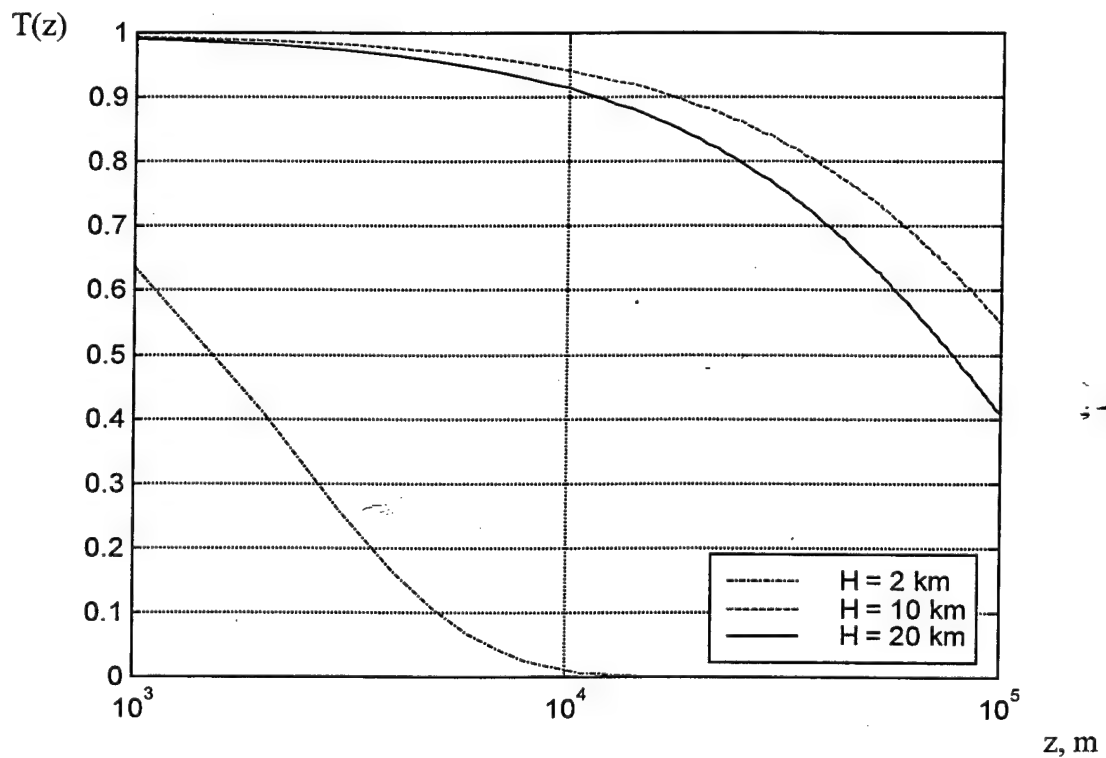


Fig.3 Horizontal profiles of atmospheric transmission at different elevation heights. Desert aerosol type.

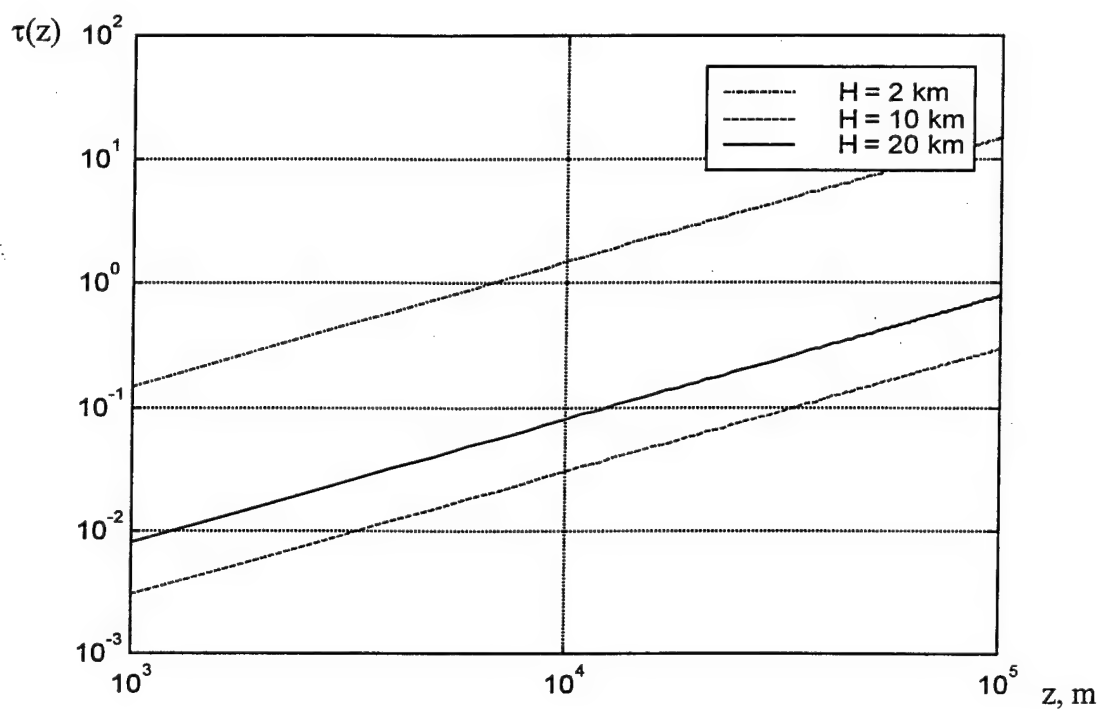


Fig. 4. Horizontal profiles of optical depth at different elevation heights. Average continental aerosol type.

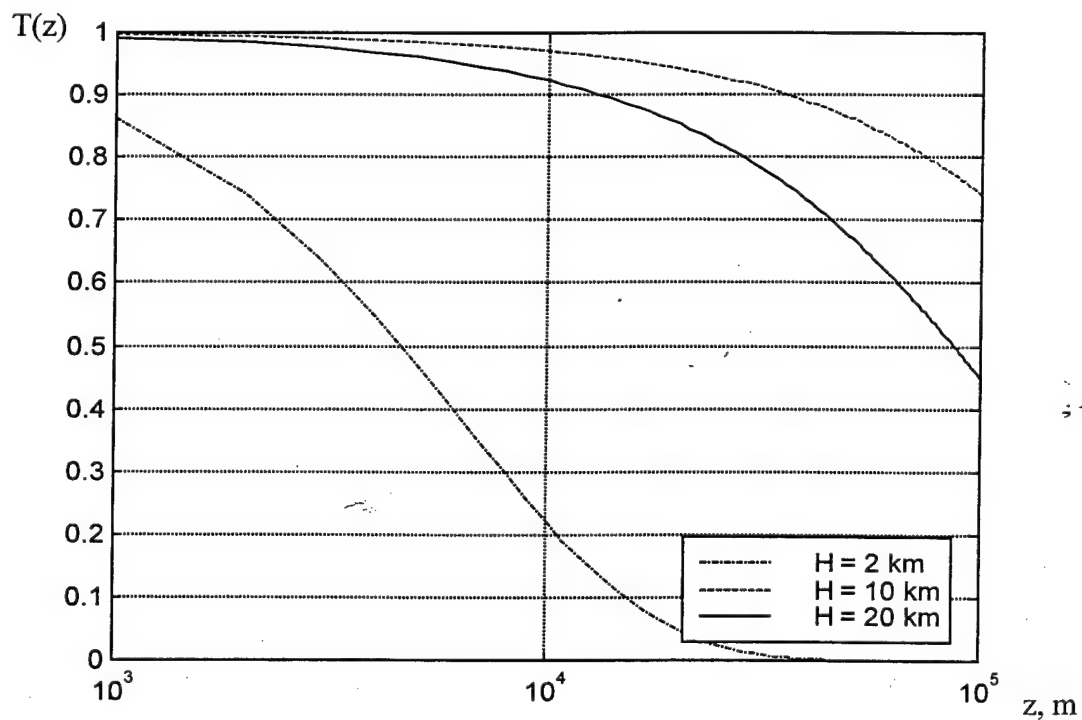


Fig. 5. Horizontal profiles of atmospheric transmission at different elevation heights. Average continental aerosol type.

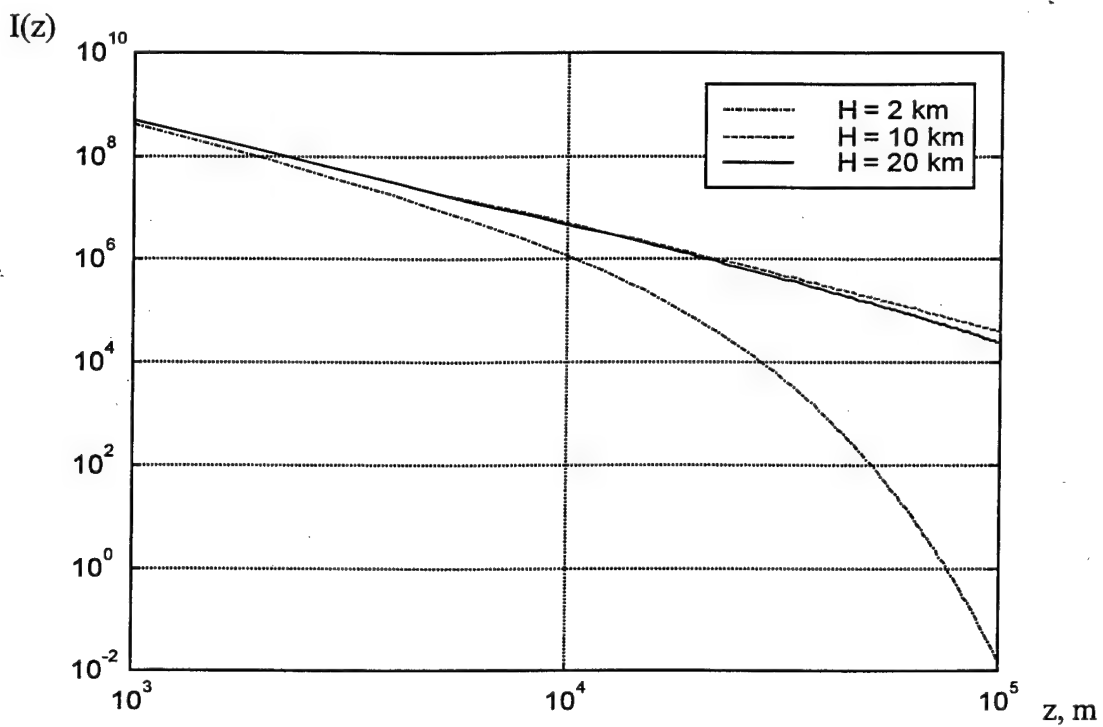


Fig. 6. Horizontal profiles of laser irradiance (Watt / m^2) in the target plane at different elevation heights for transmitter energy of 1 J (7 ns pulse). Average continental aerosol type.

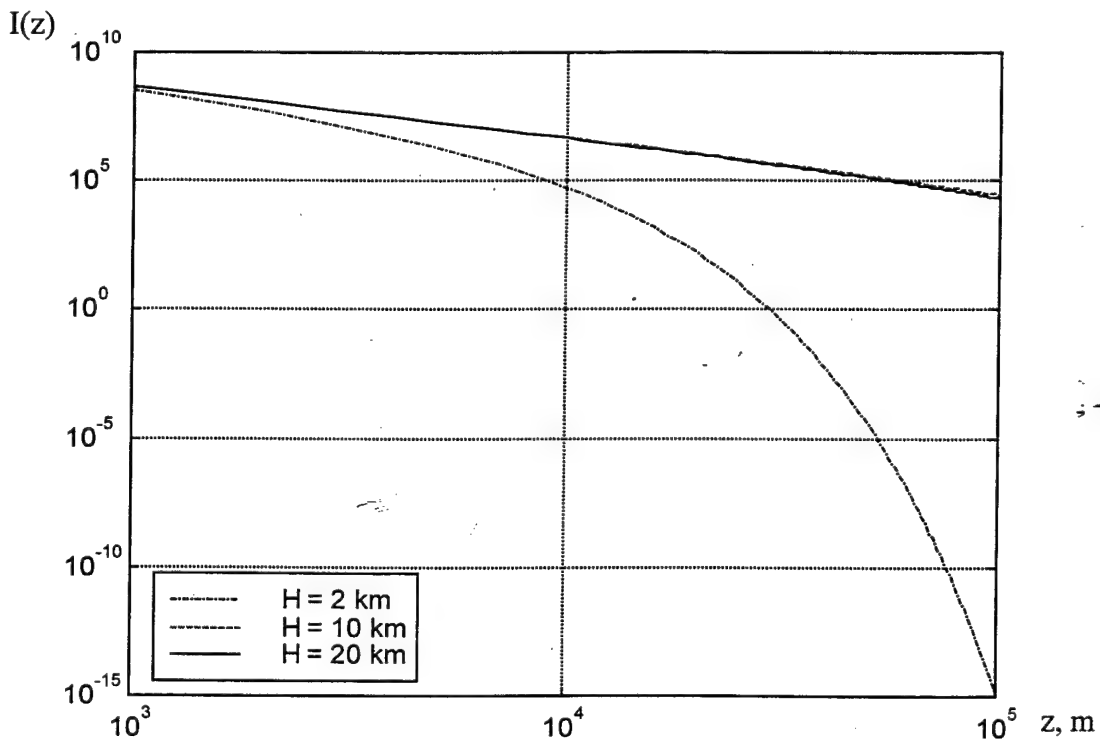


Fig. 7. Horizontal profiles of laser irradiance (Watt / m^2) in the target plane at different elevation heights for transmitter energy of 1 J (7 ns pulse). Desert aerosol type.

3. Laser beam spreading in the atmosphere.

The effect of the atmosphere on the intensity of the laser beam in the target plane is to spread the laser beam out because of turbulent and aerosol particle scattering and thus to reduce the total energy flux arriving at the target plane.

The average irradiance $\langle I \rangle$ (watt / cm²) at a distance p from the optical axis of the transmitter in a target plane located at range z is given by [8]

$$\langle I(p, z) \rangle \approx \exp[-\sigma_a \cdot z] \cdot \frac{P}{\pi W_t^2} \cdot \exp[-p^2/W_t^2] + \frac{P}{\pi W_s^2} \cdot \exp[-p^2/W_s^2], \quad (8)$$

$$\sigma_a \cdot z \gg 1,$$

where

$$W_t^2 = W_{vac}^2 + \left(\frac{2z}{k\rho_t} \right)^2, \quad (9)$$

$$W_s^2 = W_t^2 + W_a^2, \quad (10)$$

$$W_a^2 = \frac{\sigma_a \cdot z^3 \cdot \theta_{rms}^2}{3}, \quad (11)$$

$$W_{vac}^2 = W_0^2 \left[1 + \left(\frac{z}{kW_0^2} \right)^2 \right],$$

$\rho_t = (0.5 \cdot k^2 \cdot C_n^2 \cdot z)^{-3/5}$ for spherical waves, σ_a is the aerosol scattering coefficient, $k = 2\pi/\lambda$.

$\theta_{rms}^2 \equiv \langle \theta^2 \rangle$ is the mean squared scattering angle averaged over all the aerosols [6].

W_t and W_a give the contribution to the beam width due to the turbulence and aerosol scattering respectively. W_{vac} is the beam spot size in the vacuum.

The aerosol absorption and molecular scattering effects are assumed negligibly small at selected wavelengths ($>0.3 \mu\text{m}$).

For a laser beam to detect a species and targets at a long distance, the beam must not be appreciably attenuated by the intervening atmosphere. The output wavelength of the laser must therefore lie in a spectral transmission window of the atmosphere. The

most useful transparent spectral ranges are the visible (0.4-0.7 μm), near-infrared (0.7-1.5 μm), and 3 to 5 μm and 9 to 13 μm regions.

At the Nd:YAG wavelengths (1064 and 532 nm) gas absorption becomes negligible as these wavelengths are located in a propagation window where no local line absorption structure or continuum absorption bands exist.

In the first term of Eq. 8, the aerosol scattering extinguishes the intensity while turbulence spreads out the beam from its vacuum value according to Eq. 9. In the second term, scattering from aerosols further expands the beam.

Ref. [9] gives the average effective beam spot size (beam radius) for a beam with a spot size in free space, including beam spread and beam wander for the propagation path through turbulence without the aerosol contribution. It is derived from the average on-axis intensity and is given by

$$W_l = W_{vac} \left\{ 1 + 6.72k^{7/6} \cdot \Lambda \cdot m_0^{6/5} \cdot [(H - h_0)/\cos(\xi)]^{11/5} \right\}^{1/2}, \quad (12)$$

where $m_0 = \int_{h_0}^H C_n^2(h)dh$, h_0 is the laser source altitude, H is the target altitude, ξ is the

zenith angle, $\Lambda = 2z/kW_{vac}^2$, where W_{vac} is the diffraction-limited beam radius at the target plane, and C_n^2 is the turbulence structure constant ($\text{m}^{-2/3}$).

Also presented there is the average beam spot size that includes beam spread but not beam wander, i.e., the physical radius of the effective propagating beam,

$$W_n = \left[W_l - 1.96W_{vac}^2 \cdot \left(\frac{1}{2\omega_0} \right)^{1/3} \cdot k \cdot z \cdot \Lambda \cdot m_0 \right]^{1/2}, \quad (13)$$

where ω_0 is the transmitted beam radius.

In Figs. 8-21 expected laser beam spot size versus distance in vacuum with the turbulence and particle scattering contributions for different aerosol types and turbulence strengths are presented. The turbulence strength vertical profiles are given in a previous report (December 1998).

In these calculations the laser wavelength is assumed to be 532 nm. In general it was found that the laser beam widening caused by aerosols is very significant,

even more so and sometimes considerably more so, than that caused by turbulence. However, the aerosol widening is very wavelength dependent. When effective particle radius is larger than wavelength, laser beam widening caused by aerosols diminishes.

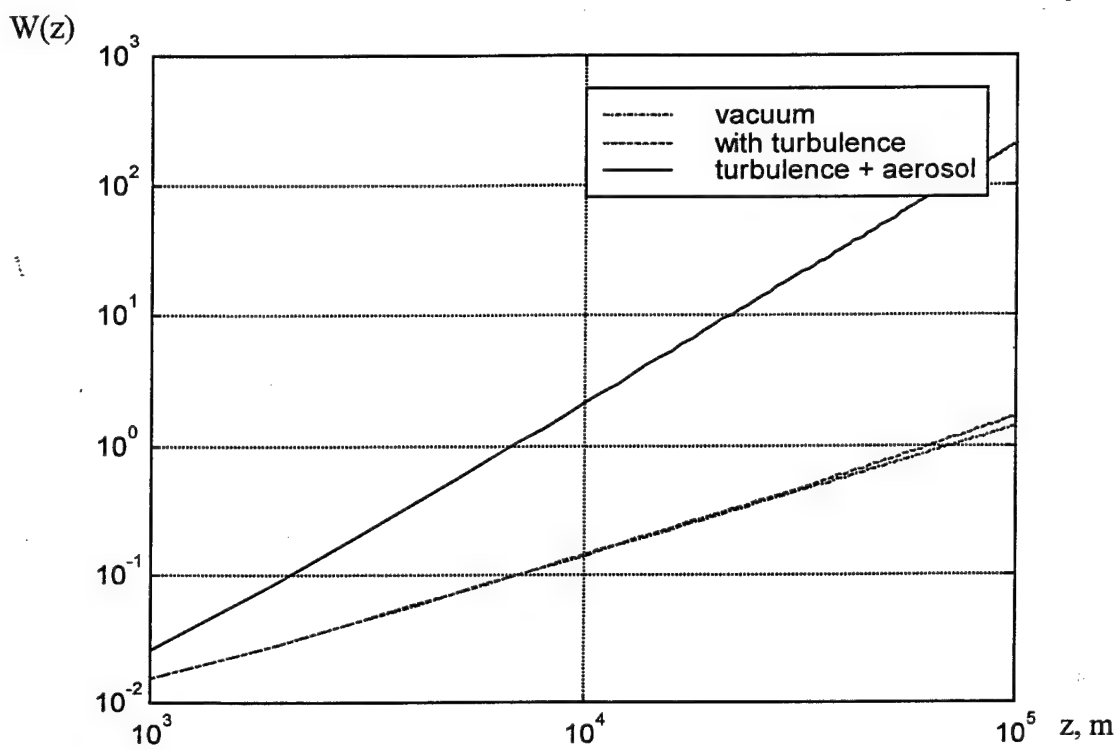


Fig. 8. Laser beam spot size (m) as a function of horizontal distance at 2 km altitude.
Average continental aerosol type. $C_n^2=1.1e-16 \text{ m}^{-2/3}$ (daytime SLC model).

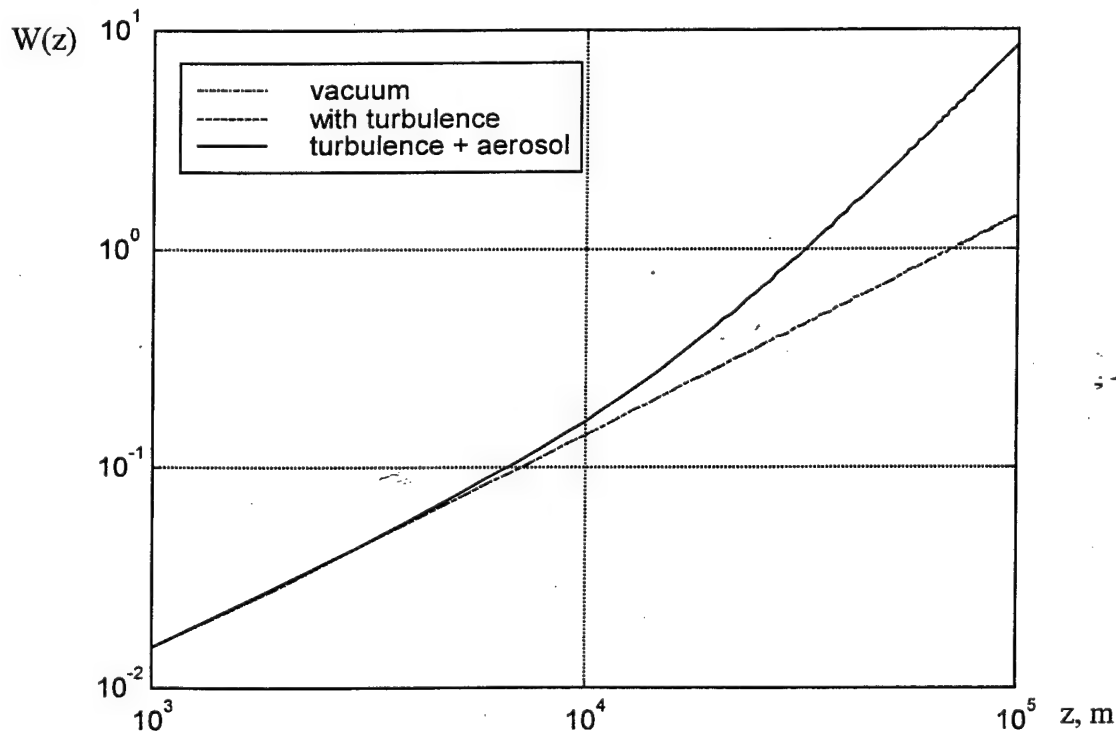


Fig. 9. Laser beam spot size (m) as a function of horizontal distance at 10 km altitude.
Average continental aerosol type. $C_n^2=2e-18 \text{ m}^{-2/3}$ (daytime SLC model).

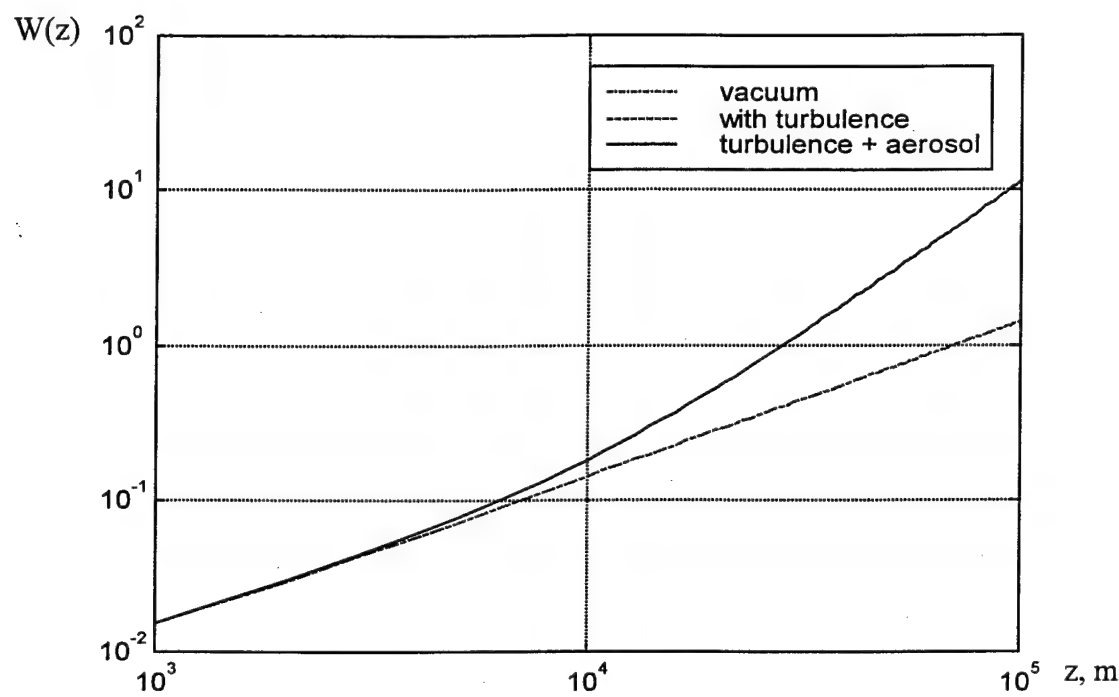


Fig. 10. Laser beam spot size (m) as a function of horizontal distance at 20 km altitude. Average continental aerosol type. $C_n^2=1.41e-18 \text{ m}^{-2/3}$ (daytime SLC model).

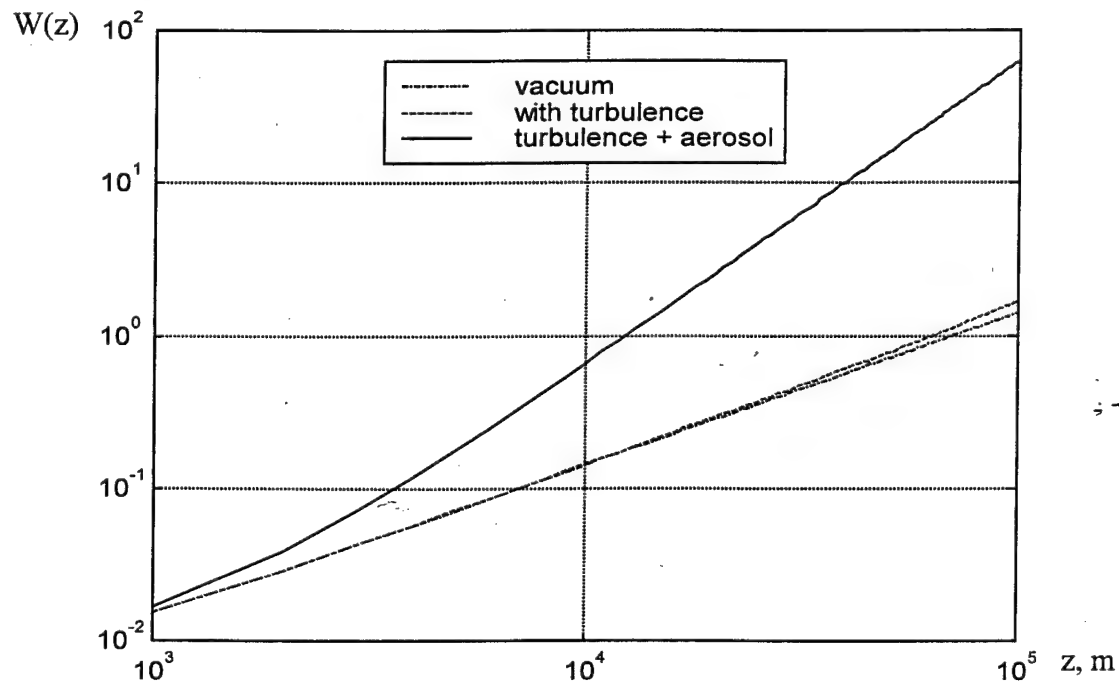


Fig. 11. Laser beam spot size (m) as a function of horizontal distance at 2 km altitude. Desert aerosol type. $C_n^2=1.1e-16 \text{ m}^{-2/3}$ (daytime SLC model).

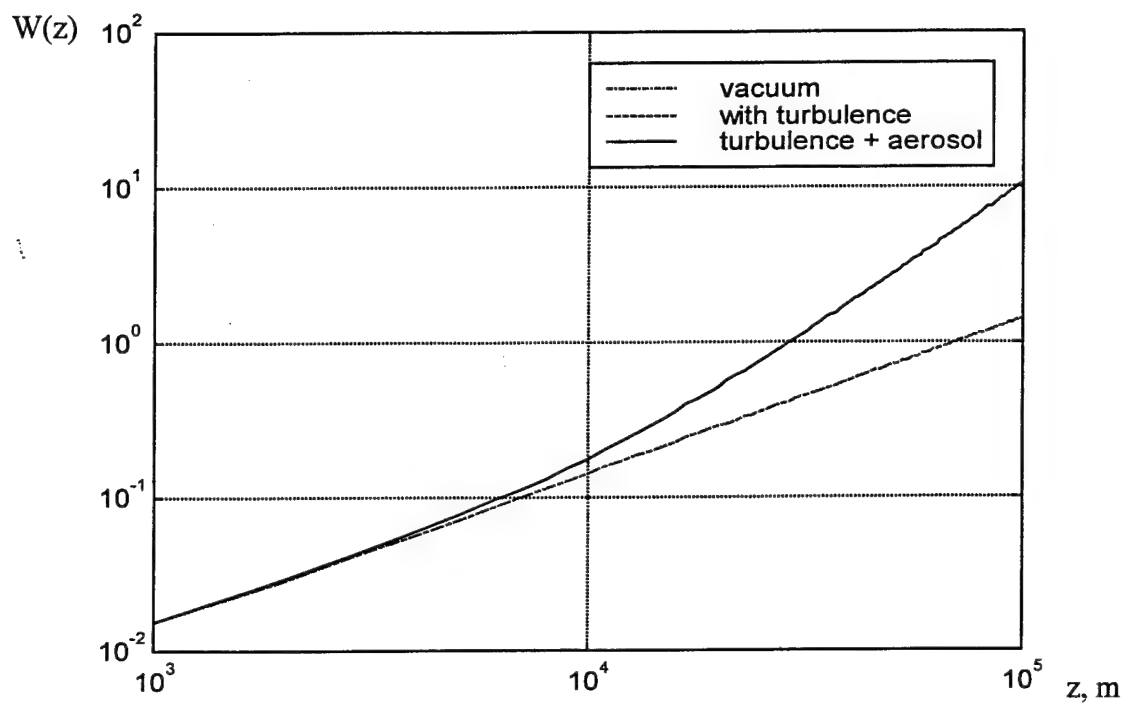


Fig. 12. Laser beam spot size (m) as a function of horizontal distance at 10 km altitude. Desert aerosol type. $C_n^2=2e-18 \text{ m}^{-2/3}$ (daytime SLC model).

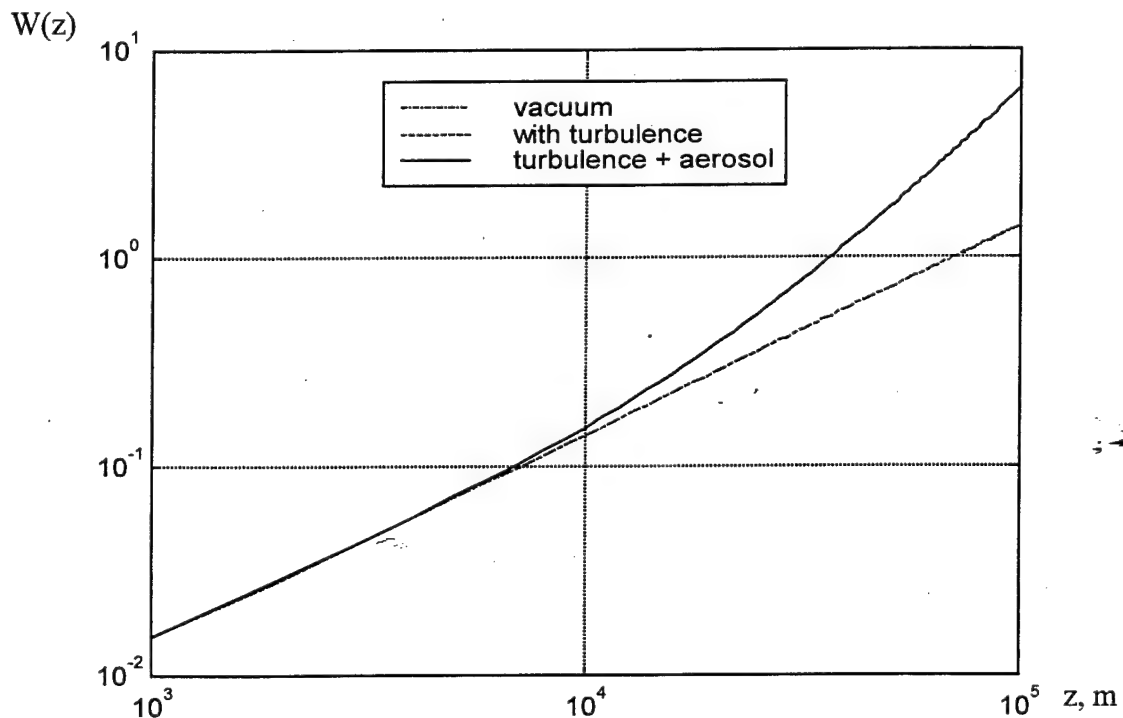


Fig. 13. Laser beam spot size (m) as a function of horizontal distance at 20 km altitude. Desert aerosol type. $C_n^2=1.41e-18 \text{ m}^{-2/3}$ (daytime SLC model).

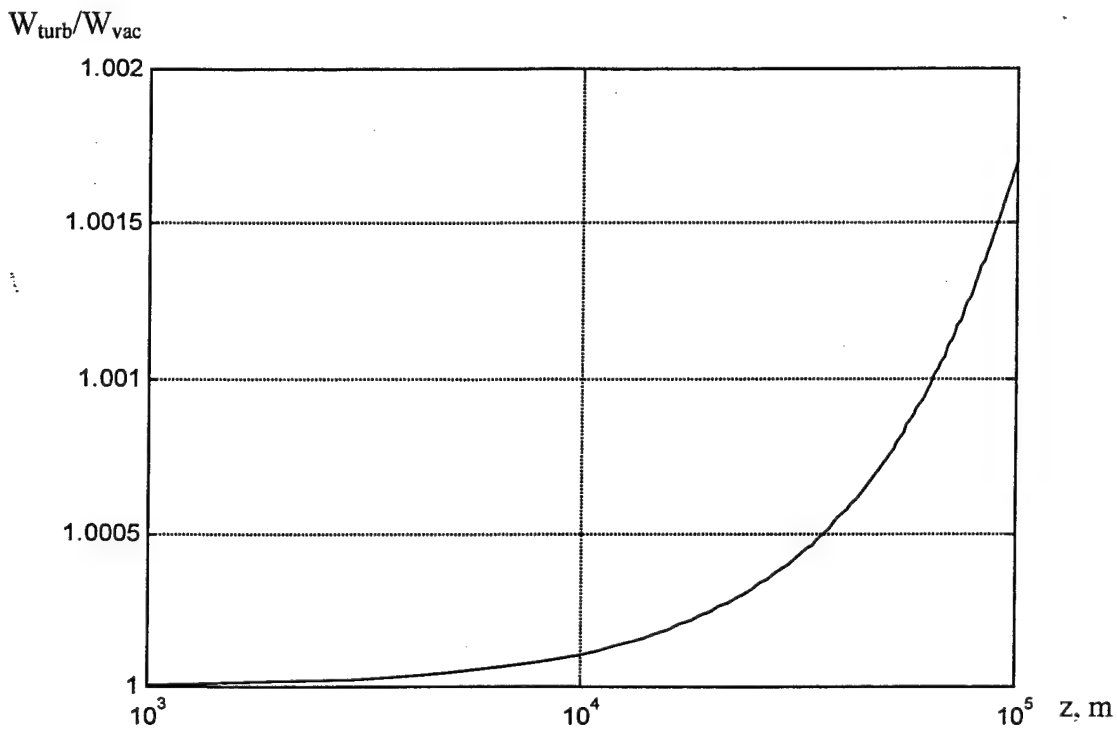


Fig. 14. Ratio of beam spot size with turbulence widening compared to that in vacuum as function of horizontal distance at 10 km altitude. Desert aerosol type. $C_n^2 = 2e-18 \text{ m}^{-2/3}$ (daytime SLC model).

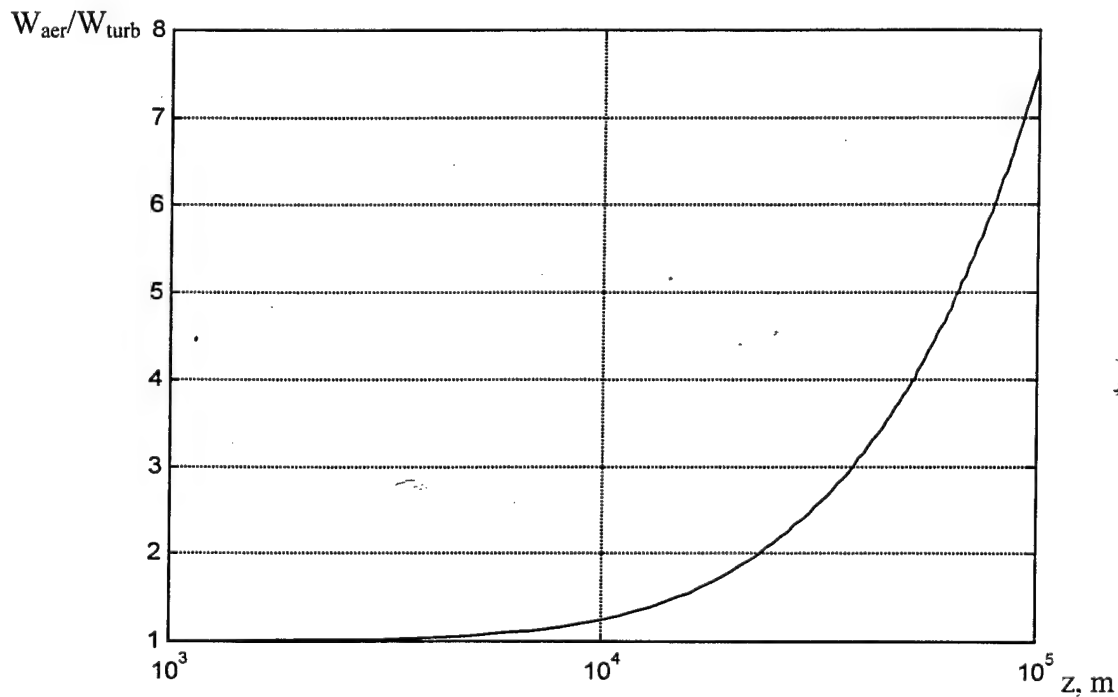


Fig. 15. Ratio of beam spot size with aerosol widening compared to turbulence widening as function of horizontal distance at 10 km altitude. Desert aerosol type. $C_n^2 = 2e-18 \text{ m}^{-2/3}$ (daytime SLC model).

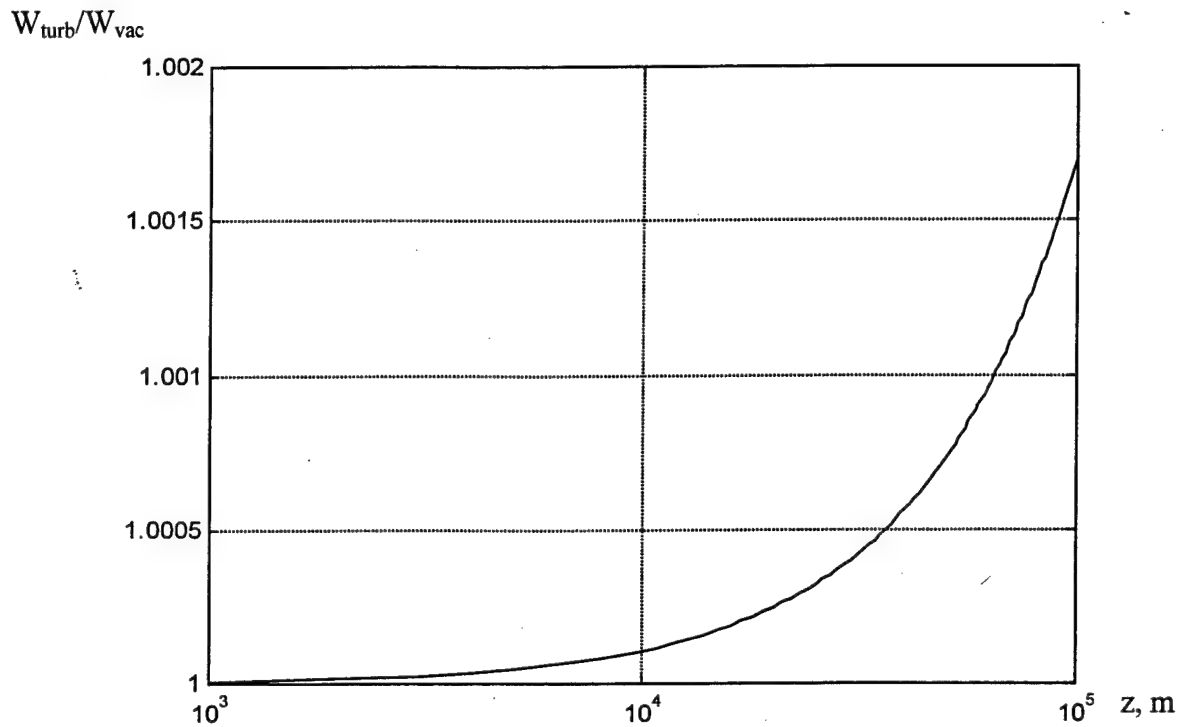


Fig. 16. Ratio of beam spot size with turbulence widening compared to that in vacuum versus horizontal distance at 10 km altitude. Average continental aerosol type. $C_n^2 = 2e-18 \text{ m}^{-2/3}$ (daytime SLC model).

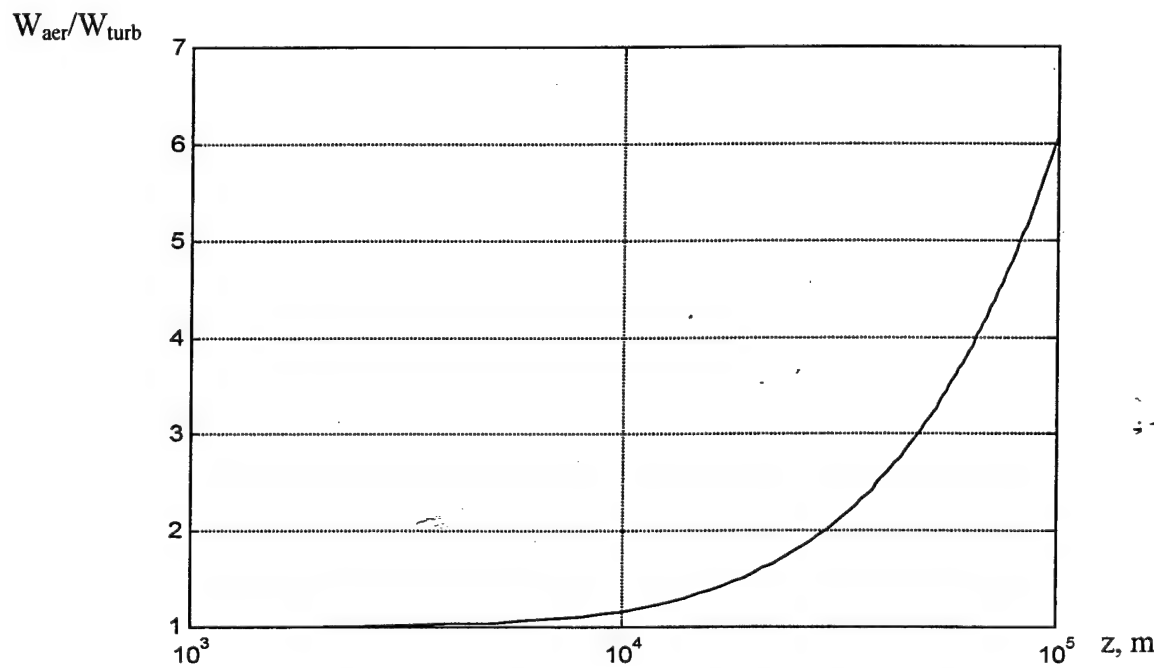


Fig. 17. Ratio of beam spot size with aerosol widening compared to turbulence widening as function of horizontal distance at 10 km altitude. Average continental aerosol type. $C_n^2 = 2e-18 \text{ m}^{-2/3}$ (daytime SLC model).

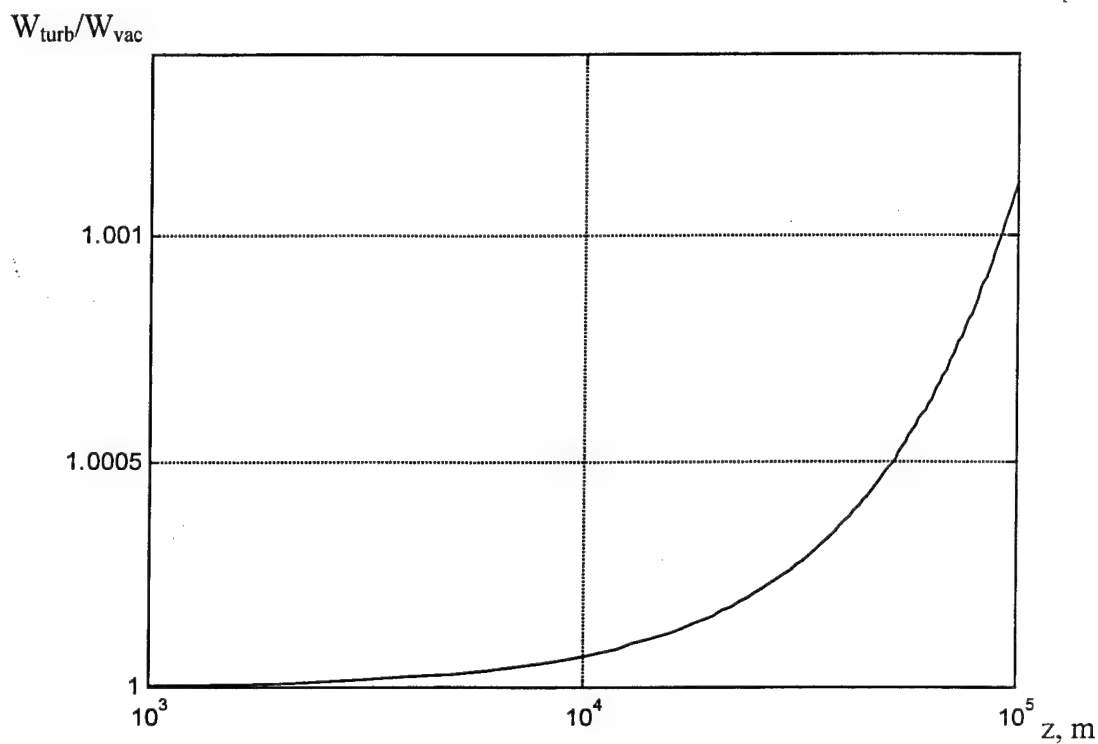


Fig. 18. Ratio of beam spot size with turbulence widening compared to that in vacuum as function of horizontal distance at 20 km altitude. Desert aerosol type. $C_n^2 = 1.41e-18 \text{ m}^{-2/3}$ (daytime SLC model).

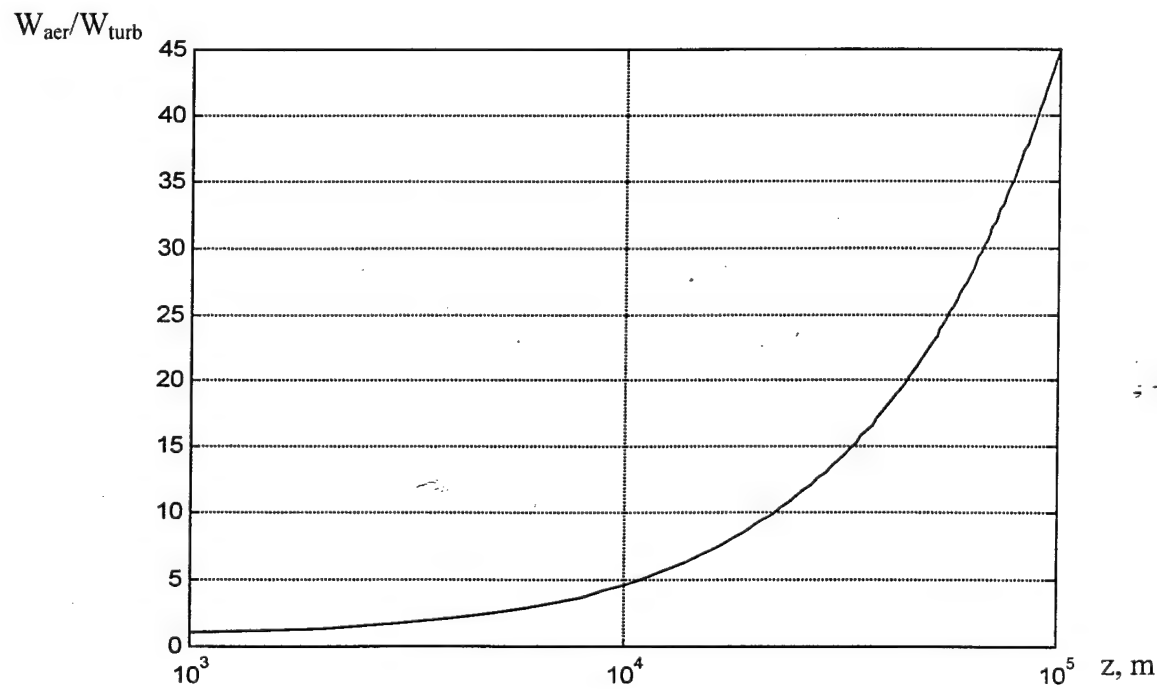


Fig. 19. Ratio of beam spot size with aerosol widening compared to turbulence widening as function of horizontal distance at 20 km altitude. Desert aerosol type. $C_n^2 = 1.41e-18 \text{ m}^{-2/3}$ (daytime SLC model).

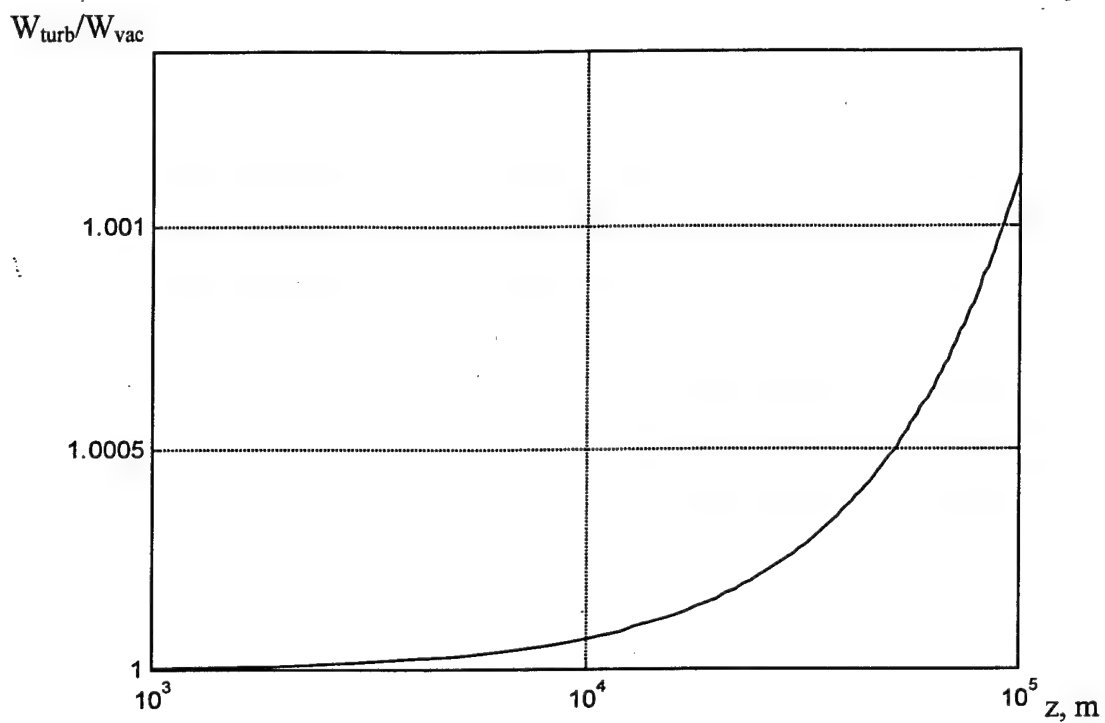


Fig. 20. Ratio of beam spot size with turbulence widening compared to that in vacuum versus horizontal distance at 20 km altitude. Average continental aerosol type.
 $C_n^2 = 1.41 \times 10^{-18} \text{ m}^{-2/3}$ (daytime SLC model).

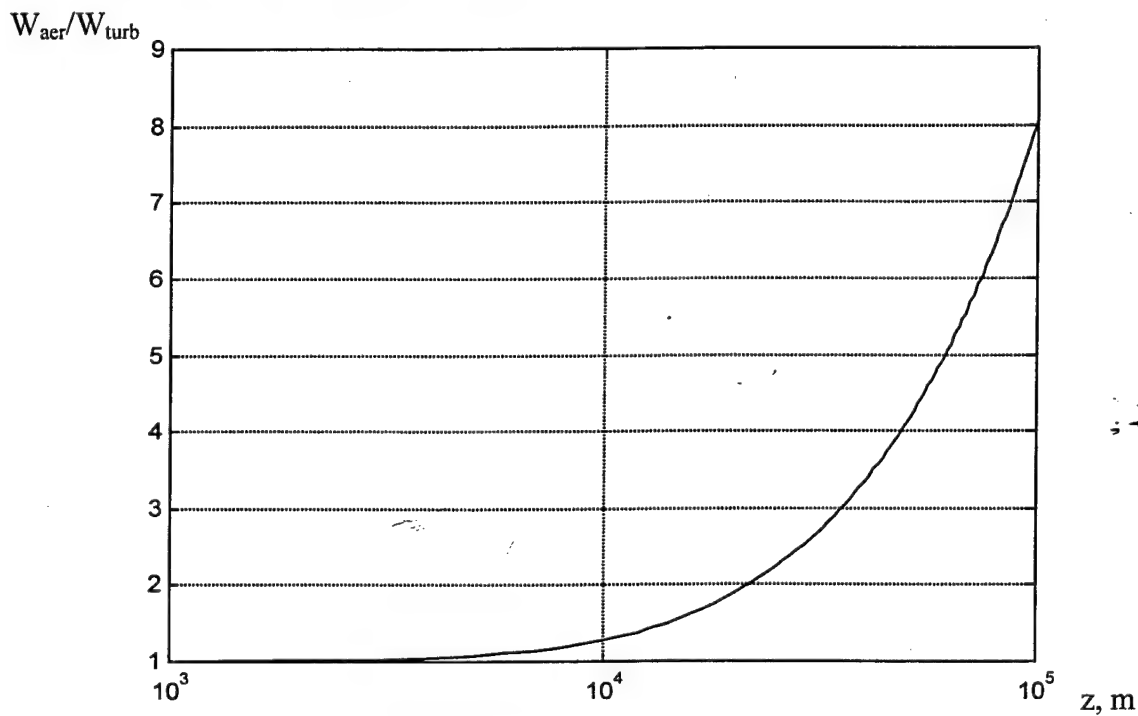


Fig. 21. Ratio of beam spot size with aerosol widening compared to turbulence widening as function of horizontal distance at 20 km altitude. Average continental aerosol type. $C_n^2 = 1.41 \times 10^{-18} \text{ m}^{-2/3}$ (daytime SLC model).

4. Lidar system discription.

The lidar we are developing to measure vertical profiles of aerosol size distribution and turbulence strength is almost ready. All the main components have been derived upon and ordered. It should be operational by the end of the year.

Fig.22 shows the schematic of the lidar setup, composed of a laser, receiving telescope, signal processing unit, and data processor. Table 4 gives the specifications of the various subsystems.

The lidar system employs a Nd:YAG laser operating on the fundamental (1064 nm), doubled (532 nm), and tripled (355 nm) wavelengths. The receiving telescope is a Classical Cassegrain design with a diameter of 12.5 inch. The optical subsystem in the telescope uses dichroic beam splitters to direct the three wavelengths to different detectors. The 532- and 355-nm channels are detected with photomultiplier tubes (PMT) operating in analog mode, and the 1064 nm channel is detected with a silicon avalanche photodiode (APD). Detected returns at all three wavelengths are to be used to calculate aerosol size distribution at each elevation range. Vertical resolution is expected to be 15 m. In addition, a cooled Intensified CCD camera (ICCD, Andor Technology) used in a novel mode as the receiver for extracting the atmospheric turbulence profiles. The ICCD has a time gating and delay that allowing to obtain a series of time- and altitude-resolved signals.

Radiation from the Nd:YAG laser is directed into the atmosphere via a right-angle prism.

The transmitting optics and the telescope are separated by approximately 1.2 m with respect to their optical axes to form a noncoaxial system. Hence the backscattered echoes are not seen by the telescope until the transmitted pulse crosses into and starts overlapping with the telescope field of view. This reduces the signal-induced noise of the PMT (induced by the strong-intensity signal from low-altitude regions, which can get superimposed with the weak signals from the high altitudes).

The overlap range may be extended for long-range probing applications (stratospheric sounding) to avoid near range signal saturation of the photodetector. Alternatively, mechanical shutters may be used to block light from reaching the detector until after some delay. Narrow-band interference filters (~1 to 2 nm bandwidths) are also included in the receiver system to reduce background radiation.

The transient signal response to each transmitted lidar pulse is sampled and digitized. Sampling rate is on the order of one sample per 100 ns (15 m resolution). Each sample is digitized with 14-bit resolution. To improve the signal-to-noise ratio, the digitized signals for each transmitted lidar pulse are averaged over tens to hundreds of pulses.

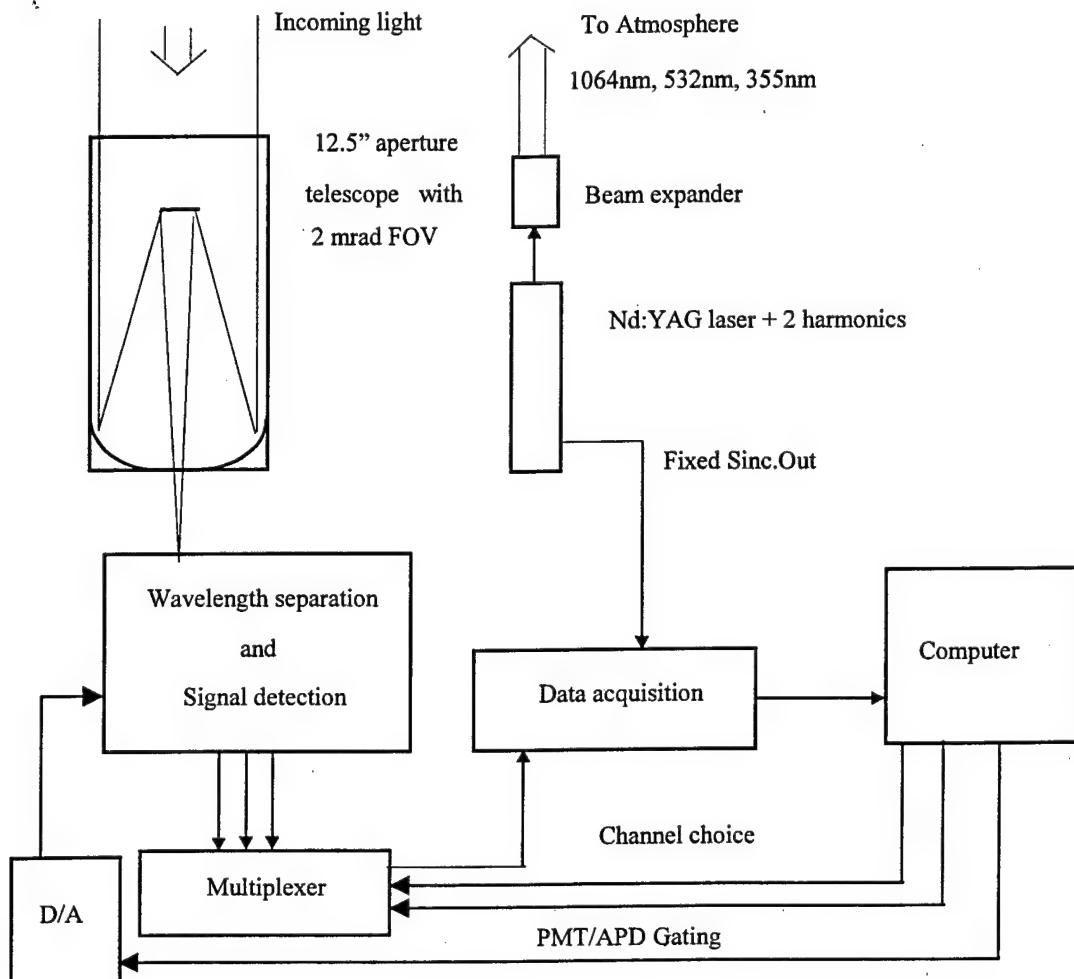


Fig. 22 Block diagram of the lidar system.

Transmitter

Laser	Nd:YAG, Continuum model Surelite I-10 with 2 harmonics
Output energy/pulse	450 mJ at 1064 nm 200 mJ at 532 nm 60 mJ at 355 nm
Repetition rate	10 Hz
Pulse duration	7 ns
Beam divergence	0.6 mrad

Receiving optics

Telescope	12.5" Classical Cassegrain (Davro Optical Systems, Inc.)
Field of view	2mrad
Filter linewidth	1nm
Filter transmittance	45% (1064nm and 532nm) 25% (355nm)

Detectors

Intensified CCD camera	Andor Technology Inc.
Photomultiplier tube	Hamamatsu R4632
Quantum efficiency	25% at 355nm 18% at 532nm
Current gain	3.5×10^6
Dark current	1nA
Excess noise factor	1.2
Avalanche photodiode	EG&G C30954E
APD quantum efficiency	30% at 1064nm
APD responsivity	36 A/W
APD excess noise factor	4
APD dark current	50nA

Signal processor

Type	Digital processing
Minimum sample rate	100 nsec
Accuracy	14 bits
Elevation resolution	15 m

Table 4. Lidar System Specifications

The lidar response may be interpreted in terms of the *lidar range equation*.

The instantaneous received power, $P(z)$, due to backscattering from height z , assuming only single scattering and a vertically pointing lidar, may be expressed in the form:

$$P(z) = P_0 \cdot G(z) \cdot \frac{ct_p}{2} \cdot \frac{A_R}{z^2} \cdot \beta(z) \cdot T^2(z), \quad (13)$$

where

P_0 = transmitted peak power,

$G(z)$ = geometry factor for overlap of transmitter/receiver beam paths,

ct_p = transmitted pulse length (t_p is the pulse duration, c is the speed of light),

A_R/z^2 = solid angle (sr) subtended by receiver aperture A_R at range z ,

$\beta(z)$ = unit volume backscattering coefficient ($m^{-1}sr^{-1}$) of the atmosphere at range z ,

$T^2(z)$ = atmospheric transmission to range z and back to the receiver.

The geometric form factor can be evaluated fairly easily for a biaxial lidar (Fig.23) if the objective lens (or mirror) of the telescope represents the limiting aperture of the receiver optics, any obstruction is neglected, and an uniform laser distribution over the area of illumination is assumed.

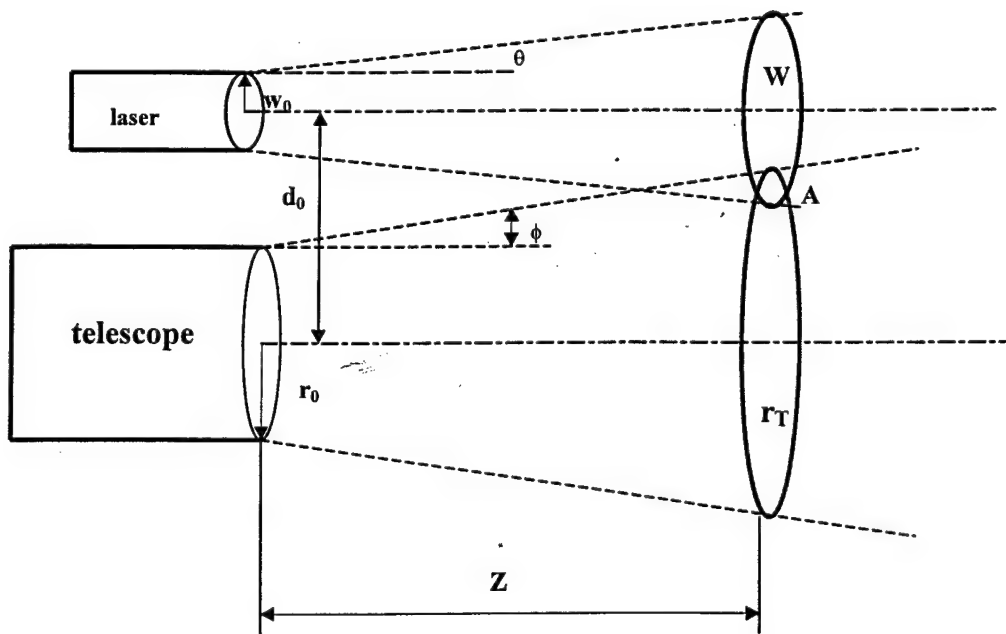


Fig. 23. Geometry of biaxial lidar.

Under the conditions of Fig.23 one can think of $G(z)$ as a simple overlap factor, and one can write

$$G(z) = \frac{A\{r_T(z), W(z); d(z)\}}{\pi W^2(z)}, \quad (14)$$

where A represents the *area overlap function*, $r_T(z)$ is the radius of the receiver optics field of view in the target plane at range z , and $W(z)$ is the radius of the circular region of laser illumination or spot at range z . In formulating these equations, the field of view of the receiver optics in the target plane is assumed a circle of radius

$$r_T(z) = r_0 + \phi \cdot z, \quad (15)$$

where r_0 is the effective radius of the telescope lens (or mirror), and ϕ is the receiver optics half opening angle.

As for the laser beam radius, assuming the output of the laser is predominantly in the TEM_{00} mode, one can write

$$W(z) = \sqrt{W_0^2 + \theta^2 \cdot z^2}, \quad (16)$$

where W_0 is the laser output aperture radius, and θ is the laser's half divergence angle.

The separation of the telescope and laser axes in the target plane is

$$d = d_0 - z \cdot \delta, \quad (17)$$

where d_0 is the separation of the axes at the lidar, and δ is the inclination angle between the laser and the telescope axes.

Three situations are possible:

1. The separation of the axes is small enough that either the area of laser illumination lies totally within the receiver optics field-of-view and correspond to an overlap factor equal to unity. This amounts to saying that if $d < |r_T - W|$ than the overlap

factor may be computed as the ratio of areas. That is $G(z) = \frac{\pi r_T^2(z)}{\pi W^2(z)} \approx \left(\frac{\phi}{\theta}\right)^2$.

2. The separation of the axes is too large for there to be any overlap between the receiver optics field-of-view and the area of laser illumination, that is, $A=0$ if $d > r_T + W$.
3. The separation of the axes lies between these extremes:

$$|r_T - W| < d < r_T + W.$$

Under these circumstances the area overlap function is

$$A\{r_T, W, d\} = W^2 \cdot \psi_W + r_T^2 \cdot \psi_r - r_T \cdot d \cdot \sin(\psi_r), \quad (18)$$

where

$$\psi_W = \arccos\left[\frac{d^2 + W^2 - r_T^2}{2Wd}\right], \quad \psi_r = \arccos\left[\frac{d^2 + r_T^2 - W^2}{2r_T d}\right]. \quad (19)$$

Clearly, the overlap factor $G(z)$ will depend on the range z and on the values of the angular parameters δ , θ , and ϕ .

The feature of a biaxial arrangement of the lidar system can be useful in eliminating near-field scattering – an effect that can saturate the photodetector when the lidar is designed for long-range measurements. Thus, for the laser and telescope axes being parallel (i.e., $\delta = 0$), the variations of $G(z)$ with z for three values of d_0 (0.8 m, 1 m, and 1.2 m) are presented in Fig. 24.

The behavior of overlap factor $G(z)$ with changing half the opening angle of the telescope, ϕ , are presented in Fig. 25, where ϕ varies between 1 and 3 mrad. The laser divergence half angle $\theta = 0.3$ mrad.

The behavior of $G(z)$ with an inclination between the telescope and laser axes is presented in Fig. 26

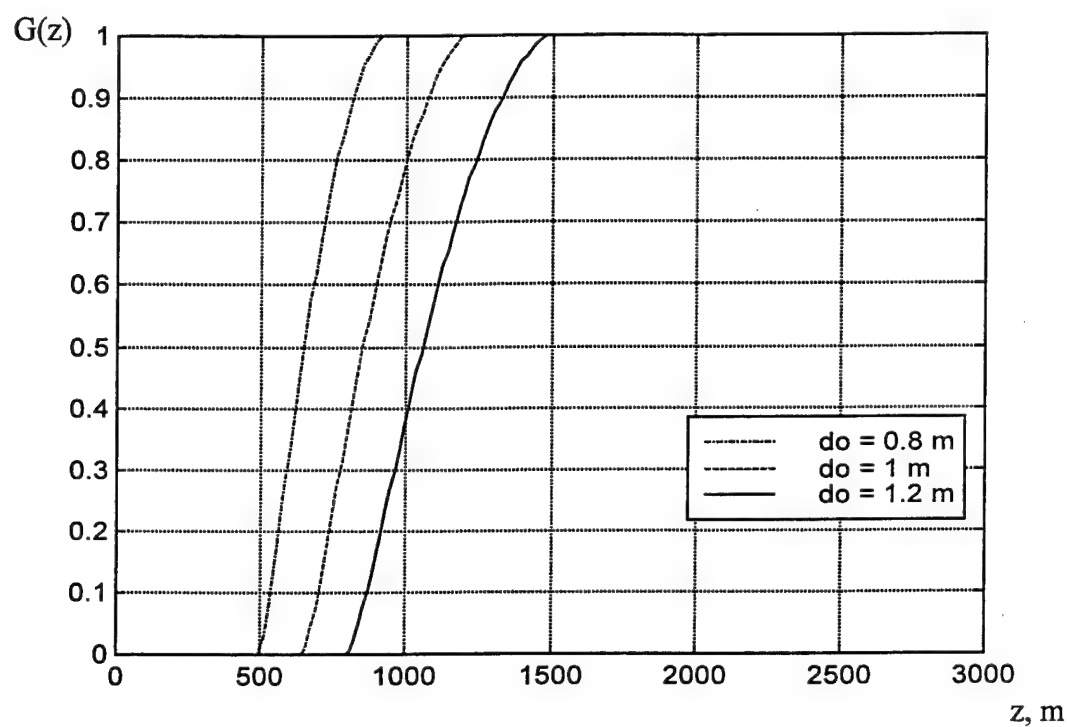


Fig.24. Variation of overlap factor $G(z)$ with range z for different separation of axes at lidar d_0 . The receiver half opening angle $\phi=1\text{mrad}$ and $\delta=0$.

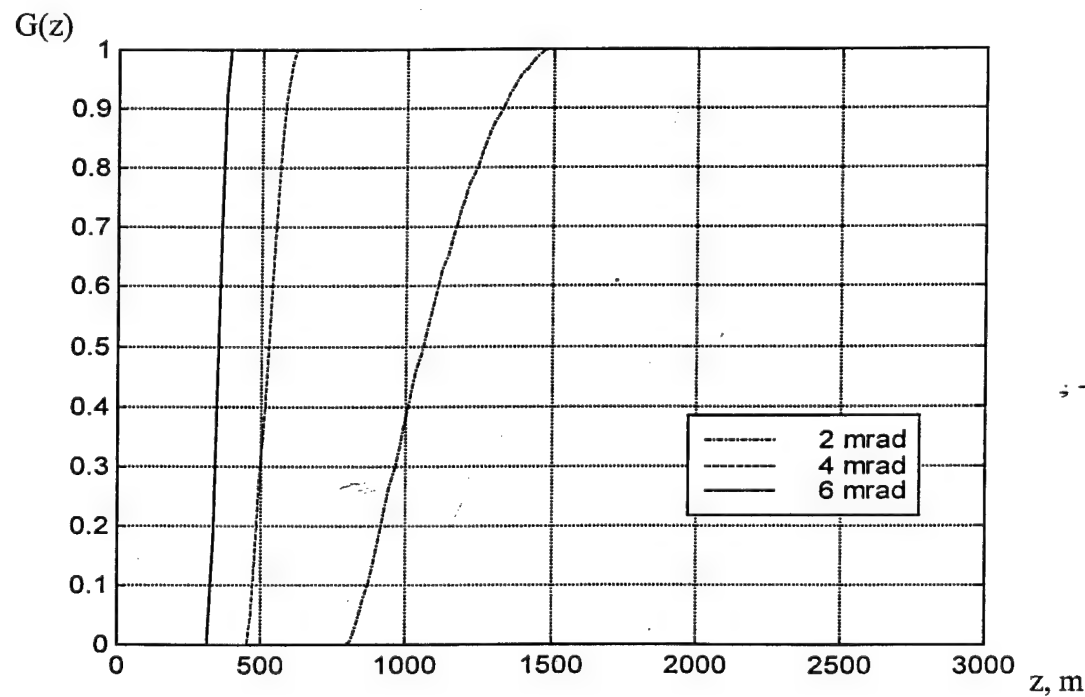


Fig.25. Variation of overlap factor $G(z)$ with z for the different receiver field-of-view $d_0 = 1.2 \text{ m}$ and $\delta=0$.

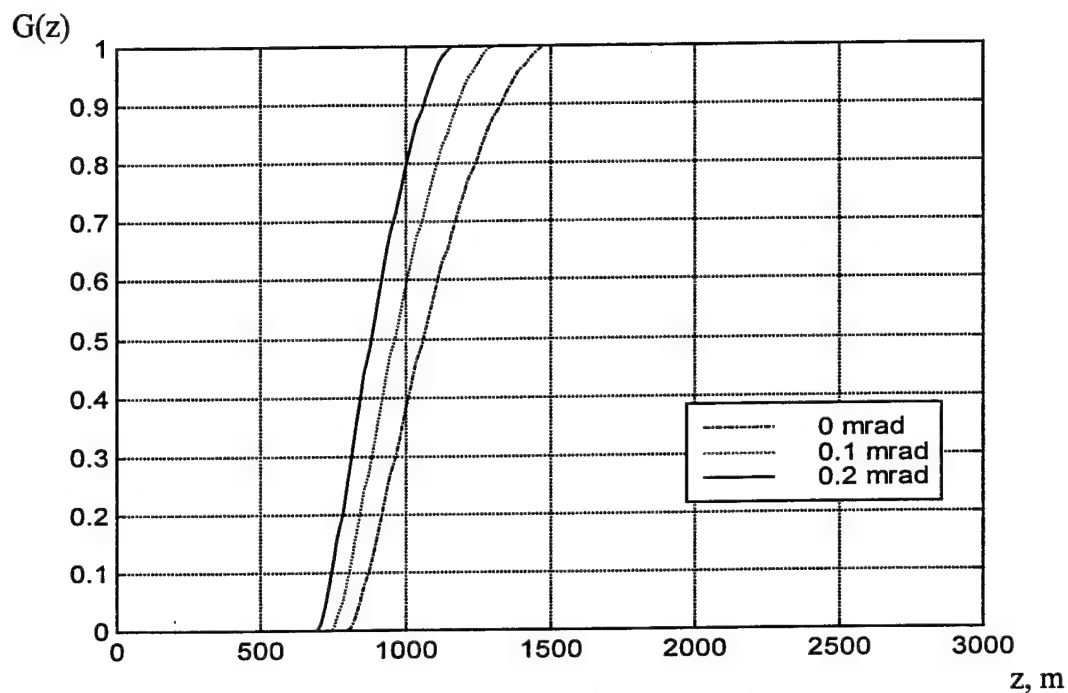


Fig. 26. Variation of $G(z)$ with range z for different inclination between telescope and laser. $d_0 = 1.2$ m and $\phi = 1\text{mrad}$.

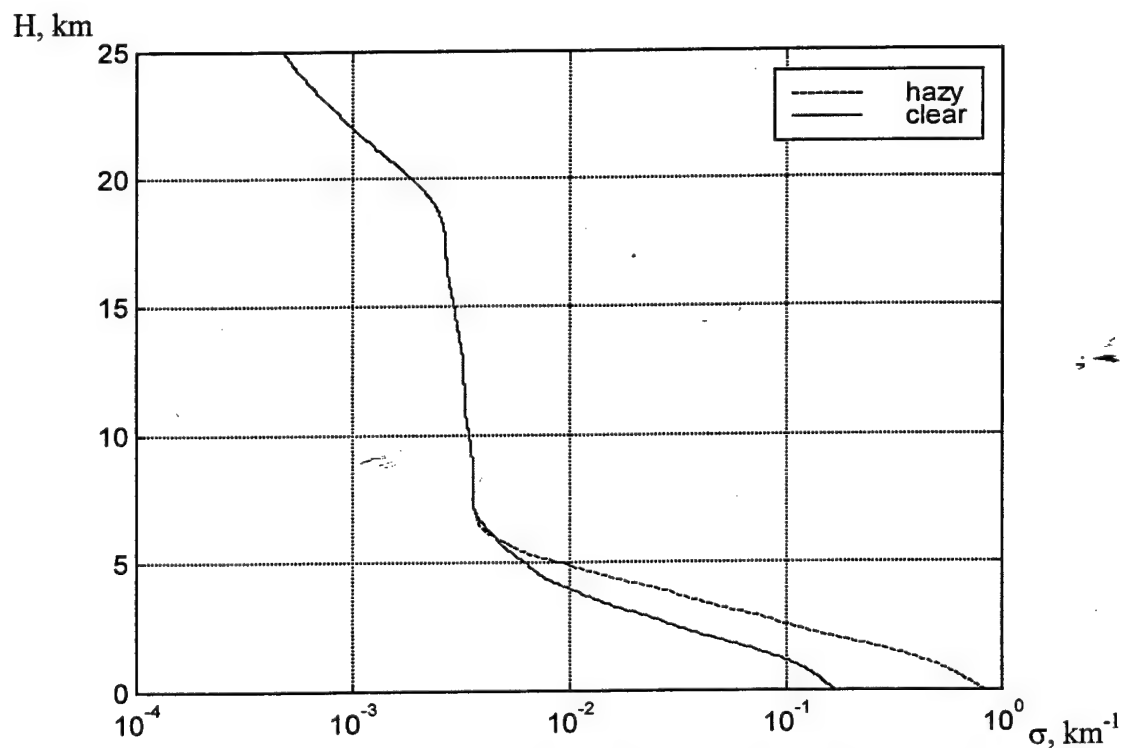


Fig. 27. Vertical aerosol extinction profiles at 532 nm used for lidar signal simulation.

These results clearly indicate that interpretation of short-range lidar measurements must take into account the geometrical factors involved.

For measurements at shorter ranges the axes of the transmitter and receiver field-of-view can be made to intersect at some finite height down to ~600 m. In this case the neutral density filter must be used in front of the detector to reduce the strong near-field radiation. Also, the detector gain can be decreased.

For the simulation of the backscattering lidar signals, two extinction profiles are selected that are considered possible cases for aerosol-polluted cloud-free atmospheres [10]. The profiles describe a "clear" and "hazy" atmosphere corresponding to visibilities of 23 and 5 km respectively at ground level. The vertical profiles of the aerosol extinction coefficient at 532 nm are shown in Fig.27.

Fig 28 shows the backscattered single-shot signal for 532 nm wavelength. The sharply rising initial portion of the signal is due to the geometrical overlap of the transmitted beam and the receiver field of view. Following system convergence the signal decreases as $1/R^2$ times the Beer's law factor.

The lidar system performance can be estimated by deriving the signal-to-noise ratio as a function of altitude.

A simple signal-to-noise ratio equation for a lidar using incoherent detection is

$$\frac{S}{N} = \frac{N_s}{\sqrt{N_s + N_b + N_e}}, \quad (20)$$

where $N_s = P(z) \cdot \eta \cdot \Delta t \cdot \lambda / hc$ is the number of signal photons detected in sample time Δt , N_b is the number of detected photons resulting from the background illumination in time Δt , N_e represents the noise current of the detector, and η is the detector quantum efficiency. For avalanche photodiode detector N_e is often the dominant noise source. Since a PMT detector offers high, nearly noise-free gain, N_e is usually negligibly small in that case. During night operation, N_b is also often negligibly small. In this case the dominant noise source is the statistical noise of the signal itself and $SNR \propto \sqrt{N_s}$. Fig. 29 shows the SNR versus altitude.

The goal of lidar inversion is to retrieve the optical atmospheric parameters σ and β from the return signal $P(z)$. A number of algorithms were presented in the previous report (September 1998).

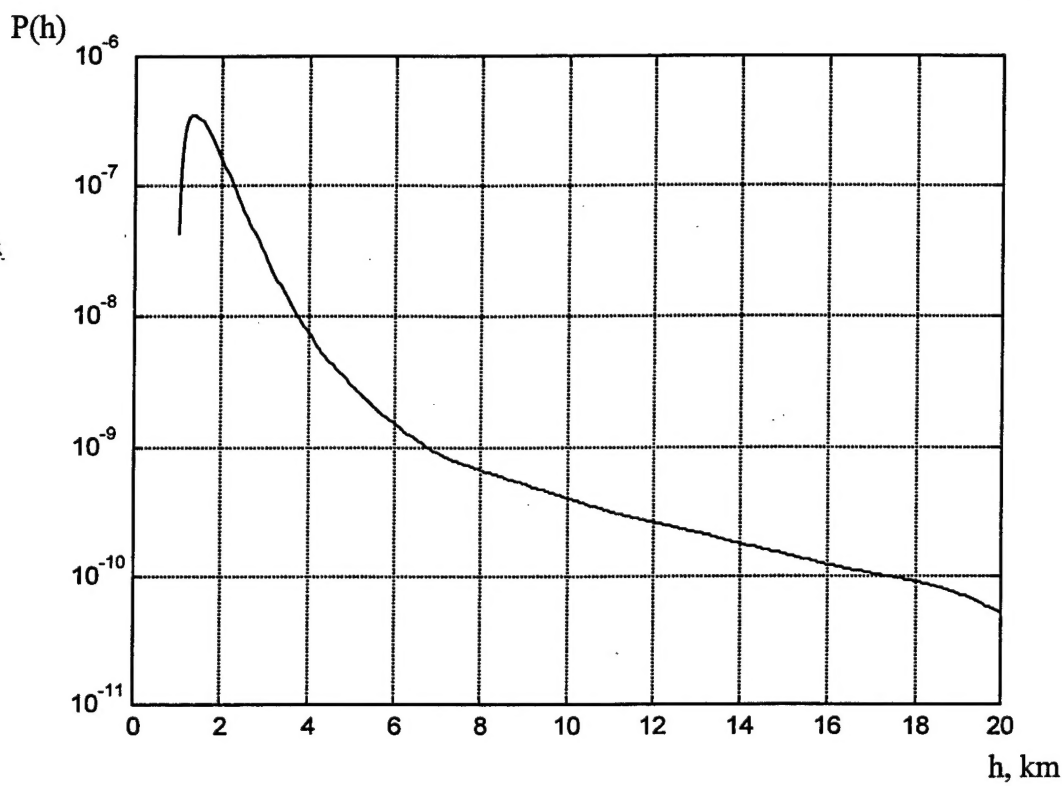


Fig. 28. Backscattered single-shot lidar signal (Watt) as a function of range.
 $\lambda=532$ nm, "Clear" atmosphere.

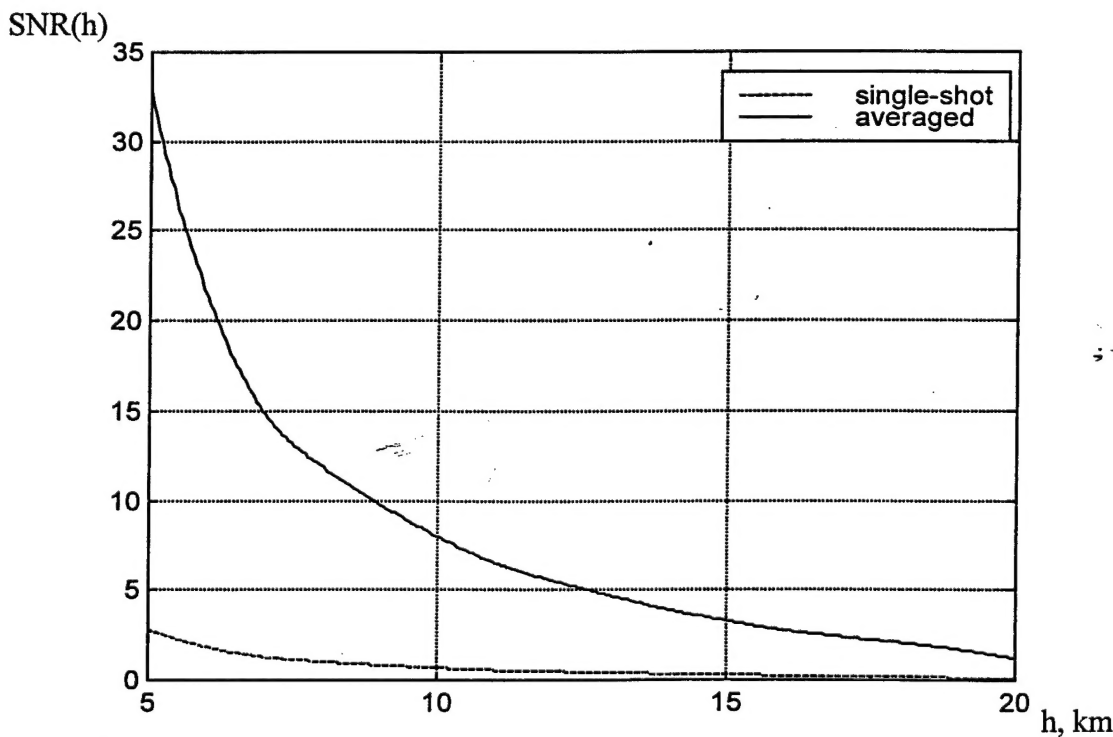


Fig. 29. Signal-to-noise ratio as function of altitude. $\lambda=532$ nm.

5. Conclusion.

Laser beam broadening for elevations studied here (2-20 km) results significantly from aerosols, usually even more so than by turbulence, as shown in Section 3 here.

References

1. D. M. Winkler, R. H. Couch, and M. P. McCormick , " An Overview of LITE: NASA's Lidar In-Space Technology Experiment", Proc. IEEE., Vol. 84, N. 2, pp. 164-179, 1996.
2. Y. Y. Gu, C. S. Gardner, P. A. Castleberg, G. C. Papen, and M. C. Kelley, "Validation of the Lidar In-Space Technology Experiment: stratospheric temperature and aerosol measurements", Appl. Opt., Vol. 36, N. 21, pp. 5148-5157, 1997.
3. J. Reichardt, U. Wandinger, M. Serwazi, and C. Weitkamp, "Combined Raman lidar for aerosol, ozone, and moisture measurements", Opt. Eng., Vol. 35, N. 5, pp. 1457-1464, 1996.
4. G. A. d'Almeida, P. Koepke, and E. P. Shettle, *Atmospheric Aerosols: Global Climatology and Radiative Characteristics*, A. Deepak Publishing, 1991.
5. E. P. Shettle and R. W. Fenn, *Models for the Aerosols of the Lower Atmosphere and the Effects of Humidity Variations on their Optical Properties*, AFGL-TR-79-0214, 1979.
6. *Atmospheric Aerosols: Their Formation, Optical Properties, and Effects*, Ed. by A.Deepak, Spectrum Press, 1982.
7. M. R. Gross, T. J. McGee, U. N. Singh, and P. Kimvilakani, "Measurements of stratospheric aerosols with a combined elastic-Raman-backscatter lidar" ,Appl. Opt. Vol. 34, N. 30. 1995.
8. R. F. Lutomirski, "Atmospheric degradation of electrooptical system performance", Appl. Opt., Vol. 17, N. 24, pp. 3915-3921, 1978.
9. R. A. Murphy and R. L. Phillips, "Reciprocal path-scattering effects for a ground-based, monostatic laser radar tracking a space target through turbulence", Appl. Opt., Vol. 36, N. 24, pp. 5996-6004, 1997.
10. R. A. McClatchey, R. W. Fenn, J. E. A. Selby, F. E. Volz, and J. S. Garing, *Optical Properties of the Atmosphere*. (Third Edition), AFCRL-72-0497, AD 753075, 1972.

REPORT DOCUMENTATION PAGE

Form Approved OMB No. 0704-0188

Public reporting burden for this collection of information is estimated to average 1 hour per response, including the time for reviewing instructions, searching existing data sources, gathering and maintaining the data needed, and completing and reviewing the collection of information. Send comments regarding this burden estimate or any other aspect of this collection of information, including suggestions for reducing this burden to Washington Headquarters Services, Directorate for Information Operations and Reports, 1215 Jefferson Davis Highway, Suite 1204, Arlington, VA 22202-4302, and to the Office of Management and Budget, Paperwork Reduction Project (0704-0188), Washington, DC 20503.

1. AGENCY USE ONLY (Leave blank)	2. REPORT DATE	3. REPORT TYPE AND DATES COVERED	
	September 1999	Final Report	
4. TITLE AND SUBTITLE Prediction of Optical Turbulence in the Stratosphere			5. FUNDING NUMBERS F6170897C0005
6. AUTHOR(S) Prof. Norman S. Kopeika			
7. PERFORMING ORGANIZATION NAME(S) AND ADDRESS(ES) Ben-Gurion University of the Negev PO Box 653 Beer-Sheva 84 105 Israel			8. PERFORMING ORGANIZATION REPORT NUMBER N/A
9. SPONSORING/MONITORING AGENCY NAME(S) AND ADDRESS(ES) EOARD PSC 802 BOX 14 FPO 09499-0200			10. SPONSORING/MONITORING AGENCY REPORT NUMBER SPC 97-4074
11. SUPPLEMENTARY NOTES			
12a. DISTRIBUTION/AVAILABILITY STATEMENT Approved for public release; distribution is unlimited.			12b. DISTRIBUTION CODE A
13. ABSTRACT (Maximum 200 words) This report results from a contract tasking Ben-Gurion University of the Negev as follows: The contractor will investigate the effects of atmospheric turbulence in the stratosphere on the propagation of optical radiation.			
14. SUBJECT TERMS EOARD, Atmospherics, Beam Propagation, Adaptive Optics			15. NUMBER OF PAGES 34
			16. PRICE CODE N/A
17. SECURITY CLASSIFICATION OF REPORT UNCLASSIFIED	18. SECURITY CLASSIFICATION OF THIS PAGE UNCLASSIFIED	19. SECURITY CLASSIFICATION OF ABSTRACT UNCLASSIFIED	20. LIMITATION OF ABSTRACT UL

NSN 7540-01-280-5500

Standard Form 298 (Rev. 2-89)
Prescribed by ANSI Std. Z39-18
298-102